Centro de Investigaciones en Óptica, A.C.

División de Fotónica

Loma del Bosque 115, Lomas del campestre 37150,
León, Guanajuato, México

Optical Spin Injection in Graphane

by

Reinaldo Arturo Zapata Peña

A thesis submitted in partial fulfillment of the requirements
for the degree of Master of Science (Optics).

Advisor:
Dr. Bernardo Mendoza Santoyo

December 18, 2012

Optical Spin Injection in Graphane

by

Reinaldo Arturo Zapata Peña

Approved:

Dr. Bernardo Mendoza Santoyo
Thesis Advisor

Dr. Norberto Arzate Plata
Second Reader

Dr. Francisco Villa Villa
Third Reader

Centro de Investigaciones en Óptica, A.C.
December 18, 2012

In memory of my father and my uncle Enrique.

I will miss you every single day of my life.

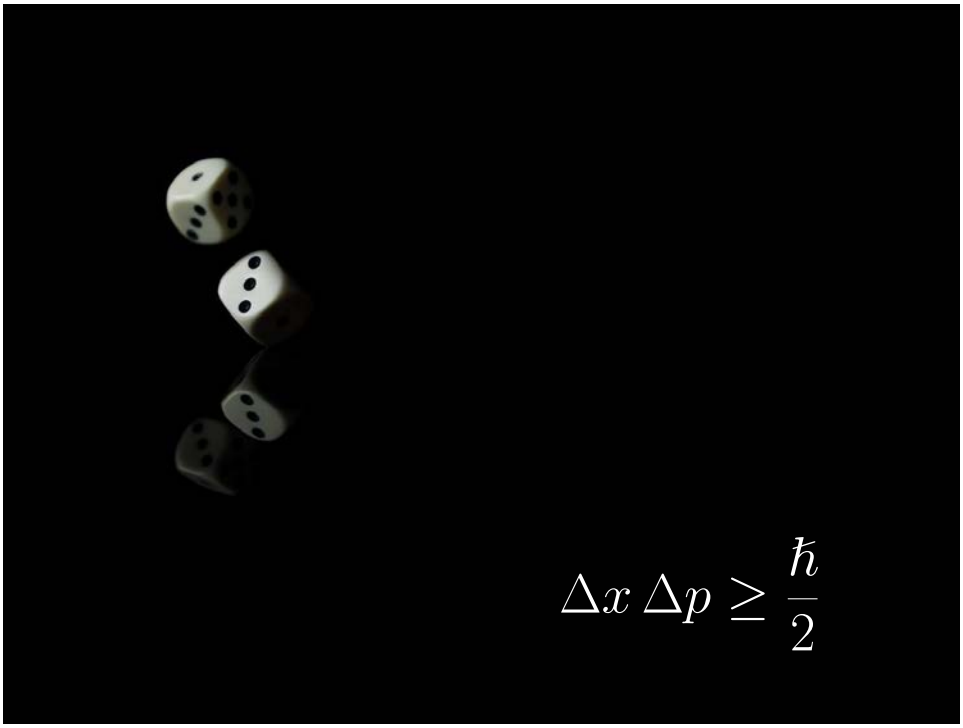

"Einstein, please quit telling God what to do".

–Niels Bohr

Dedication

To my wife

for sharing her life with me
for having the arms wide open whenever I need it
for the great upcoming moments that we are going to share.

To my daughter

for changing my life
for giving me reasons to wake up every morning
for receiving me with a smile every time I arrive home.

To my mother

. . . for bringing me to life
for being at my side in every moment
for keeping the faith in me regardless what happen.

Acknowledgements

Very special thanks to Bernardo Mendoza Santoyo:

> For being the advisor and supervisor of this thesis work. For being the responsible about my interest in Quantum Mechanics. For *teaching us* every single day how to read his articles and "the manual" since the beginning of the thesis project.

I extend a huge acknowledgement Sean “Chonito” Anderson:

> For spending his time sharing knowledge about LaTeX. For his help with the routines to make calculations of results. For all the absurd and non–absurd discussions we have in “the office.”

Special thanks to Dr. Arzate and Dr. Villa Villa:

> For being my thesis committee.

My wife Patricia, my daughter Samantha, my mom Eloisa, sisters Eloisa and Andrea, Patricia L., Miguel O. and Cecilia N. for sharing their lives with me, for the good times and for them *attentive* listening every time I say “do you really want I explain it to you?”

My friends and classmates: Marcelo, Alberto, Ramsés, Izcoatl, Pilar, and Monse. For all the time we spent together in and out the CIO.

All the people who makes possible the CIO continues being the great institution it is.

CONACyT for the financial support during the time I studied the Masters degree and for the upcoming support for the Ph.D.

Abstract

In this thesis we calculate, using *ab–initio* quantum methods, the degree of the electronic spin polarization when a circularly polarized beam incides over Graphane. The Graphane is obtained when Graphene is selectively doped with hydrogen. Graphene is a bi–dimensional material made with carbon atoms; its discoverers where awarded with the Nobel Price of Physics in 2010. We have that, for an specific hydrogen doping the electronic spin of Graphane can be totally polarized. This is a really promissory result for a large number of Spintronics applications.

En esta tesis se calcula, usando métodos cuánticos de primeros principios, el grado de polarización del espín electrónico cuando un haz polarizado circularmente incide sobre Grafano. El Grafano es obtenido del Grafeno al doparlo selectivamente con hidrógeno. El Grafeno es un material bi–dimensional de átomos de carbono; sus descubridores fueron galardonados con el premio Nobel de Física en el 2010. Se obtiene, que para un dopaje de hidrógeno específico, el espín electrónico del Grafano puede ser polarizado en su totalidad. Este es un resultado muy promisorio para un gran número de aplicaciones en la Espintrónica.

Contents

List of Figures

Chapter 1

Introduction

Contents

Graphene is a structural configuration, or allotrope of carbon consisting of planar monoatomic sheets of sp^2 bonded carbon atoms. The structure is a densely packed two–dimensional honeycomb or equilateral triangular crystal lattice [1] with a carbon–carbon chemical bond length of 0.142 nm [2]. Early work on the subject by Hanns–Peter Boehm [3, 4] dates back to 1962 with his paper on single layer carbon foils.

1.1 Generalities of Graphene and Graphane

Graphene has some interesting properties – fractional quantum Hall effect at room temperature [5–7], ambipolar electric field effect along with ballistic conduction of charge carriers [8], tunable band gap [9] and high elasticity [10]. Other noteworthy properties are extreme mechanical strength and thermal conductivity in two–dimensional films, electronic characteristics like Dirac particles with linear dispersion, its transport energy gap, and its optical absorption coefficient [1, 11]. Ideal graphene is a perfectly flat, single layer material; this is generally not the case as ripples occur due to thermal fluctuations [1].

Thanks to these diverse properties, graphene became one of the most relevant research topics in condensed matter physics and material science for the last eight years [1, 2, 12–14] since its first synthesis in 2004. In 2010 the Nobel Prize in Physics was awarded to Andre Geim and Konstantin Novoselov for their groundbreaking work in this field[1].

[1] Nobel Foundation announcement of Nobel Price, 2010.

Recent studies on the aforementioned properties and the structural and electronic properties of carbon–based materials have created a wide array of applications for graphene. Carbon–based nanostructures (such as nanotubes) are ideal for hydrogen storage due to their large surface area [15]; hydrogen is a promising new fuel for automobiles and can potentially be exploited in smaller devices. Multi–layered graphene also has applications, such as bi–layer graphene that creates a band gap when an external electric field is applied [16, 17].

Graphene sheets are mainly produced by shaving graphene flakes off bulk graphite and depositing them on a SiO_2/Si substrate. However, the size and crystalline quality are not easily controlled. Other groups have grown graphene sheets epitaxially on SiC (0001) [18] but these layers have inconsistent thickness.

The monolayer graphene sheet shown in Fig. (1.1) is considered the basic building block of all graphitic forms. Keeping the sp^2 hybridization, the 2D carbon sheets can be wrapped up into 0D fullerenes (Fig. 1.2a), rolled into 1D nanotubes (Fig. 1.2b), or stacked into 3D graphite (Fig. 1.2c). Graphite consists of a large number of graphene sheets stacked one over the other with an average interplanar spacing of 0.335 nm. Table 1.1 is a comparison of different parameters between different dimensions of carbon–based structures.

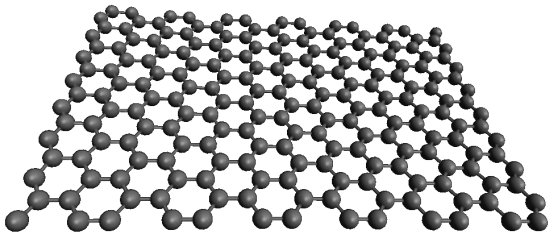

Figure 1.1: A monolayer graphene sheet.

Graphene samples with few of layers are being investigated with equal interest. According to our interest we can define three different types of grapheneswith one, two or some few layers (less than ten). Although single–layer graphene and bi–layer graphene were first obtained by micromechanical cleavage [8] and graphenes containing different numbers of layers have been

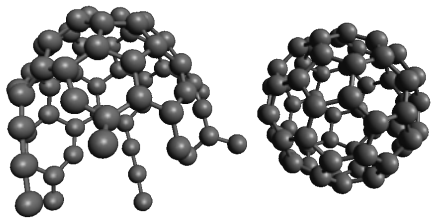

(a) Graphene sheet wrapping into fullerene.

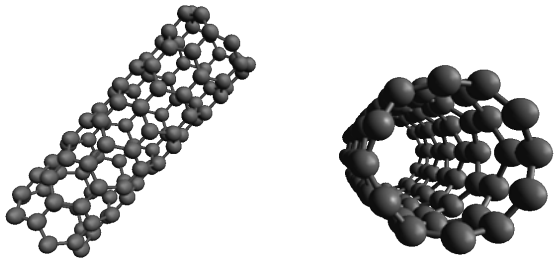

(b) Carbon nanotube with honeycomb lattice.

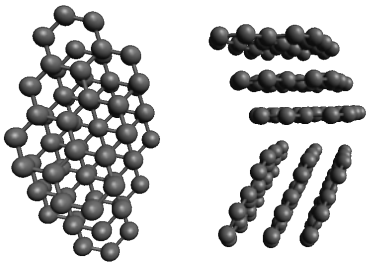

(c) Graphite.

Figure 1.2: Graphitic forms obtained from graphene.

Dimensions	0	1	2	3
Isomer	fullerene	nanotube	graphene	diamond
Hybridisation	sp^2	sp^2	sp^2	sp^3
Density	1.72	1.2 - 2.0	2.26	3.515
Bond length (Å)	1.40	1.44	1.42	1.54
Conductivity	semiconductor	metal or semiconductor	zero gap semiconductor	insulator
Band gap (eV)	$E_g = 1.9$	$E_g \approx 0.3 - 1.1$		

Table 1.1: Comparison between carbon–based compounds of different dimensionalities.

obtained using different methodologies [2, 19, 20]. There are other reports of the properties of few–layer graphene.

Graphene has been characterized by a variety of microscopic and physical techniques including atomic force microscopy, transmission electron microscopy, scanning tunneling microscopy and Raman spectroscopy [1–5].

Using the atomic force microscopy technique the number of graphene layers can be observed directly [2, 13]. Also the Transmition Electron Microscopy is a useful procedure to determine the morphology and structure of graphene like is depicted in Fig. 1.3a [21]. Raman spectroscopy is an important tool that can be used to characterize graphene samples; also it can provide information about the quality and number of layers in a given sample as shown in Fig. 1.3b [22–26]. An unespected result is that the single–layer graphene placed on a Si wafer with a 300 nm thick layer of SiO_2, becomes visible under the optical microscope [2, 13, 14].

As was mentioned before, from the structure of graphene most of the graphitic forms can be obtained. Also, planar polycyclic aromatic hydrocarbons with only benzenoid hexagonal rings, could be considered as fragments of a graphene sheet with the peripheral atoms saturated with hydrogen, and thus provide molecular models of graphene segments. Graphene segments have interest from the scientific and technological perspectives. Moreover, planar polycyclic aromatic hydrocarbons or graphene segments themselves are of great research interest because they are widely found in the residues of domestic and natural combustion of coal, wood, and other organic material that include chemical bonds between C, H, O and other elemements. Their unique electronic properties providing opportunities for novel functionalized nanomaterials and nanodevices [27]. Understanding the mechanism of formation of graphene segments is necessary to control its formation and in

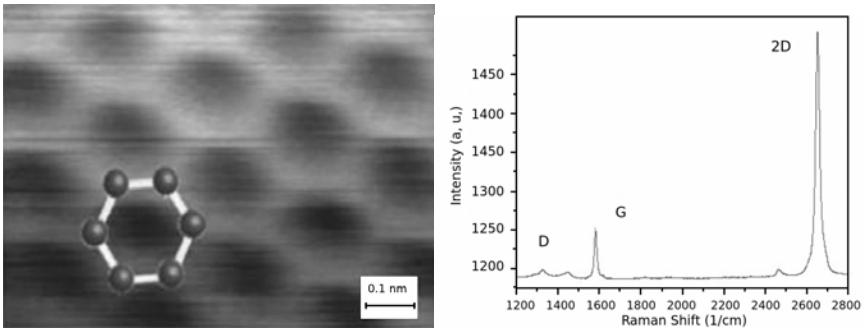

(a) (b)

Figure 1.3: (a) Image took with the technique of Transmision Electron Microscopy and (b) Raman spectrum of single–layer graphene, prepared by micromechanical cleavage.

turn, to meet its application requirements.

The role of hydrogen has been studied during the chemical vapor deposition of carbon materials [28] including graphene and diamond. There are some reports on the phenomena of luminescence in various chemical vapor deposited diamond and a-C:H films [29–33]. Visible photoluminescence has been observed in carbon nanoclusters embedded in a SiO_2 matrix [34] and from C_{60} thin films [35]. Unlike a -Si:H, the photoluminescence efficiency of a -C:H film is high and it shows luminescence even at room temperatures [36–39]. A clear understanding of the luminescence phenomenon would help to produce high–quality luminescent films by a proper control of the experimental conditions [40].

As was supposed to be, at the beginning, a large number of the studies about graphene have been in the direction of synthesis of single–layer graphene and few–layer graphene using different techniques. Some of those techniques are presented in the next section of this chapter.

1.2 About this thesis

This thesis which has the title “Optical Spin Injection in Graphane” is part of our research under the supervision of Dr. Bernardo Mendoza Santoyo while I was studying the Master in Science at *Centro de Investigaciones en Óptica, A.C.* León, Guanajuato México.

The first objective is to present some of the properties of a recent topic of scientific research in semiconductors and solid state physics: graphene and graphane (hydrogenated graphene). The second one is to develop the background quantum theory to describe and characterize anisotropic media and describe optical spin injection. The third and last one consists of the computational calculations to characterize the spin injection in the $C_{16}H_{16}$–*chair* (Fig. 4.1a) and $C_{16}H_8$–*up* (Fig. 4.1b) graphane's molecules.

To achieve the first objective in chapter 1 we presented some chemical and mechanical procedures that can be followed to obtain the graphene and graphane molecules. Also we presented the functionalization and some chemical, electronical and optical properties. Both molecules are depicted in Fig. (4.1).

In chapter 3 we present the quantum theory to reach the second objective. In this chapter we present the Density Functional Theory and the Spin–Density Theory (section 3.3) and how the Bloch's theorem (section 3.4.2) together with the Plane Waves Expansion (section 3.5) helped us to characterize the Optical Spin Injection. The main results of the chapter 3 correspond to the equations from (3.71) to (3.75).

In sections 4.1.1 and 4.1.2 we present the software ABINIT and TINIBA. This software was used to attain the last objective of characterize the properties of the graphane molecules previously mentioned.

Results and conclusions can be found, respectively, in sections 4.4 and 5.1.

Chapter 2

Properties

In this chapter we present some extended properties of Graphene and Graphane.

2.1 Synthesis

2.1.1 Single–Layer Graphene

The first structure of our subject of study was the single–layer graphene. Initially it was prepared by micromechanical cleavage from a high order pyrolytic graphite [8]. When this procedure is done, a layer is peeled of from the crystal of high order pyrolytic graphite simply using a scotch tape and later transferring it to a silicon substrate. Is important to say that when this method is used the size and crystalline quality are not easily controlled [41].

A better technique to obtain the single–layer graphene is using a chemical method that involves the reduction of single layer–graphene oxide dispersion in dimethylformamide with hydrazine hydrate [42]. The stirring procedure is as follows: graphite oxide is first prepared by an oxidative treatment of graphite by employing the Hummers procedure [43], by the reaction of graphite powder (500 mg) with a mixture of concentrated H_2SO_4 (12 ml) and $NaNO_3$ (250 mg) in a 500 ml flask kept in an ice bath. While stirring the mixture, 1.5 g of $KMnO_4$ is added slowly and the temperature brought up to 308 K. After stirring the mixture for 30 minutes, 22 ml of water is slowly added and the temperature raised to 371 K. After 15 minutes, the reaction mixture is diluted to 66 ml with warm water and treated with 3% of H_2O_2. Then the suspension so obtained is filtered to obtain a yellow–brown powder. This is washed with warm water. Graphite oxide readily forms a stable colloidal suspension in water and the suspension is subjected to ultrasonic treatment (300 W, 35 KHz) to produce single–layer graphene oxide.The single–layer graphene oxide suspension (0.3 mg/ml) in a H_2O + N,N-dimethylformamide

mixture (50 ml) is treated with hydrazine hydrate at 353 K for 12 h [42]. This yields a black suspension of reduced graphene oxide; to make a stable dispersion of it, a further amount of N,N-dimethylformamide is added to the suspension.

In comparison of this technique with the micromechanical cleavage of graphite is important to mention that the crystalline quality and size of the resulting structure is improved, making the reduction of single–layer graphene oxide produces a material that can contain some residual oxygen functionalities [44].

Quantities in the order of grams of single–layer graphene have been obtained by a solvothermal procedure using sodium and ethanol [45].Also, exfoliation of graphite in N–methylpyrrolidone or a surfactant/water solution employing ultrasonication yields stable single–layer graphene dispersions [46, 47].

Single–layer graphene is also prepared using chemical vapor deposition by decomposing hydrocarbons on films or sheets. Single–layer graphene films are produced on the Si terminated (0001) face of single–crystal 6H-SiC, a kind of Silicon Carbide crystal, by thermal desorption of Si [48–50]. In this procedure, the substrates are subjected to electron bombardment in ultra-high vacuum at temperature near to 1300 K to remove oxide contaminants and then heated to temperatures ranging from 1523 to 1723 K for periods from one to twenty minutes. Single–layer graphene is prepared more conveniently making the chemical vapor deposition in films of transition metals such as Ni, Cu, Co, and Ru [51] by decomposing a variety of hydrocarbons such as methane, ethylene, acetylene, and benzene. The number of layers variate depending on which hydrocarbon is used and reaction parameters.

In reference [52] there were used different transition metals to grow graphene by decomposing the variety of hydrocarbons mentioned. In those experiments, nickel and cobalt foils with thickness of 0.5 mm and 2 mm, respectively, were used as catalysts. These foils were cut into $5 \times 5\,\mathrm{mm}^2$ pieces and polished mechanically. The chemical vapor deposition process carried out by decomposing hydrocarbons around 1073 – 1273 K. By employing a nickel foil, the chemical vapor deposition was carried out by passing methane (60 – 70 sccm[1]) or ethylene (4 – 8 sccm) along with a high flow of hydrogen around 500 sccm at 1273 K for 5 – 10 minutes. With benzene as the hydrocarbon source, benzene vapor diluted with argon and hydrogen was decomposed at 1273 K for 5 minutes. On a cobalt foil, acetylene (4 sccm)

[1]The flow measurement term, sccm, means *Standard Cubic Centimeters per Minute*.

and methane (65 sccm) were decomposed at 1073 – 1273 K, respectively. In all these experiments, the metal foils were cooled gradually after the decomposition. In Fig. (2.1) a schematic diagram of growing procces of graphene is shown and h-Bn films using chemical vapor deposition [52].

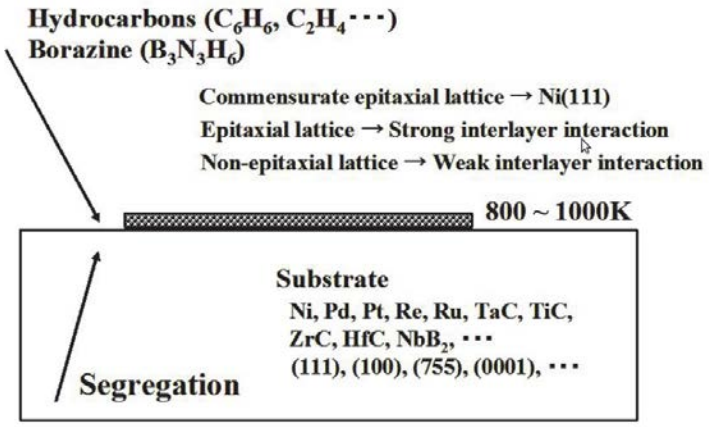

Figure 2.1: Schematic diagram to obtain graphene and h-BN films by chemical vapor deposition.

2.1.2 Few–Layer Graphene

An important method to prepare few–layered graphene is by thermal exfoliation of graphitic oxide at high temperatures [53, 54]. In this method, graphitic oxide is first prepared by the Staudenmaier method. This method starts with a mixture of, sulfuric acid (10 ml) and nitric acid (5 ml) that is put in a 250 ml reaction flask cooled in an ice bath. Graphite (0.5 g) is added under vigorous stirring to the acid mixture. After the graphite powder is fully dispersed, potassium chlorate (5.5 g) is added slowly over fifteen minutes. The reaction mixture is stirred for 96 h at room temperature. On completion of the reaction, the mixture is filtered and the residue of graphitic oxide is washed in a 5% solution of HCl. Graphitic oxide is then washed repeatedly with deionized water until the pH of the filtrate is neutral and then dried in vacuum at 333 K. Graphitic oxide so prepared (0.2 g) is placed in an alumina boat and inserted into a long quartz tube sealed at one end. The sample is purged with Ar for ten minutes, and then the quartz tube is quickly inserted into a tube furnace preheated to 1323 K and kept

in the furnace for 10 minutes. The sample obtained after this procedure corresponds to the few–layers graphene.

Another method of preparing few–layers graphene is by reacting single–layer graphene oxide in water with hydrazine hydrate at the refluxing temperature or by microwave treatment [19, 55]. In this method 1 ml of hydrazine hydrate is added to 100 ml of stable aqueous exfoliated graphene oxide solution (1 mg/1 ml) and refluxed for twenty four hours. The reduced graphitic oxide turns black and precipitates at the bottom of the flask. The resulting precipitate is filtered and washed with water and methanol. Instead of using hydrazine hydrate one can also use ethylene–glycol as a reducing agent to prepare few–layers graphene. In this procedure, the homogeneous mixture of 25 ml of exfoliated graphene oxide and 2 ml of ethylene–glycol is taken in a 50 ml PTFE–lined bomb. The sealed autoclave is kept in an oven at 443 K for twenty four hours under autogenous pressure and allowed to cool room temperature gradually. The product is washed with water and ethanol.

Graphene can be prepared, like was mentioned before, by heating nanodiamond in an inert or a reducing atmosphere, condition in which oxidation is prevented by removal of oxygen and other oxidising gases. The effect of heating nanodiamond at different temperatures has been studied by Enoki et al., [56, 57]. Annealing of nanodiamond at high temperatures in an inert atmosphere produces few–layered graphene [54–56]. In reference [44] were treated that procedure in detail. In the preparation, using nanodiamond particles by soaking in concentrated HCl before using in order to avoid contamination with magnetic impurities. Then was heated 100 mg of pristine nanodiamond powder (particle size 4 – 6 nm, Tokyo Diamond Tools, Tokyo, Japan) placed in a graphite container and was heated in a graphite furnace in a helium atmosphere at different temperatures (1923, 2123, 2323 and 2473 K) for one hour.

In general, graphene synthesized by chemical vapor deposition has a high quality and a large area. This is attributable to multiple factors: the growth mechanism on transition metal surfaces, the multi–crystalline nature of the catalyst substrate, and the simultaneous nucleation of carbon atoms from multiple sites of the substrate surface. Therefore, scientific research is required in order to fabricate high quality graphene with large single crystal domains. Recent experimental experiments showed the domain formation of chemical vapor deposition when synthesized graphene and the defects are present in the boundaries of the substrate [58]. There have been made many experimental researches about the growth mechanism of graphene on

the catalyst surface [59, 60] having highlighted the significance of carbon dimer super–saturation on the metal surface to initiate the nucleation of graphene.

2.1.3 Graphane

Arc evaporation of graphite in the presence of hydrogen yields hydrogenated–graphene, also called graphane, with exclusively 2–3 layers. Although flake size is smaller having 100 – 200 nm [61]. This makes use of the knowledge that the presence of H_2 during arc–discharge process terminates the dangling carbon bonds with hydrogen and prevents the formation of closed structures. To prepare the hydrogenated graphene direct current arc discharge of graphite, evaporation was carried out in a water–cooled stainless steel chamber filled with a mixture of hydrogen and helium in different proportions without using any catalyst. The proportions of H_2 and He used in the experiments are, H_2 (70 torr) -He (500 torr), H_2 (100 torr) -He (500 torr), H_2 (200 torr) -He (500 torr) and H_2 (400 torr) -He (300 torr).

In a typical experiment, a piece of graphite rod (alfa Aesar with 99.999% purity, 6 mm in diameter and 50 mm long) is used as the anode and another graphite rod (13 mm in diameter and 60 mm in length) was used as the cathode. The discharge current was in the 100 – 150 A range, with a maximum open circuit voltage of 60 V. In Fig. 2.2 a transmission electron microscopy and atomic force microscopy images of the hydrogenated graphene sample are show. An important aspect of the arc–discharge method is its use in doping graphene with boron and nitrogen [62]. Boron and nitrogen doped graphene have been obtained by carrying out the discharge in the presence of H_2+diborane and H_2+ (pyridine or ammonia) respectively. In spite of the many advances made in the last four years, controlled synthesis with a desired number of layers remains a challenge.

2.2 Graphene and graphane functionalization

The functionalization of carbon nanotubes, done before the functionalization of graphene, was done by covalent and non–covalent procedures in order to disperse or solubilize them in different solvents [63, 64]. Later, functionalization of graphene took similar strategies. Acid–treated graphene containing surface -OH and -COOH groups was first reacted with $SOCl_2$ to create

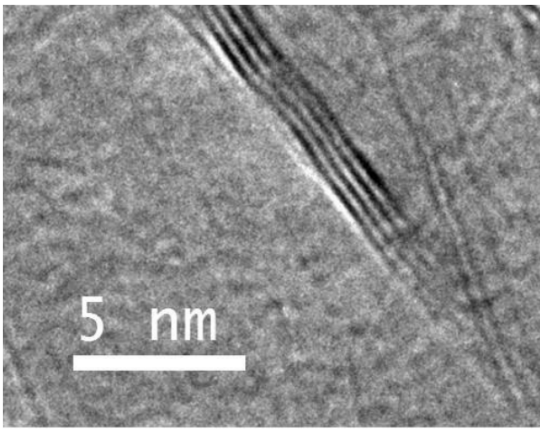

(a)

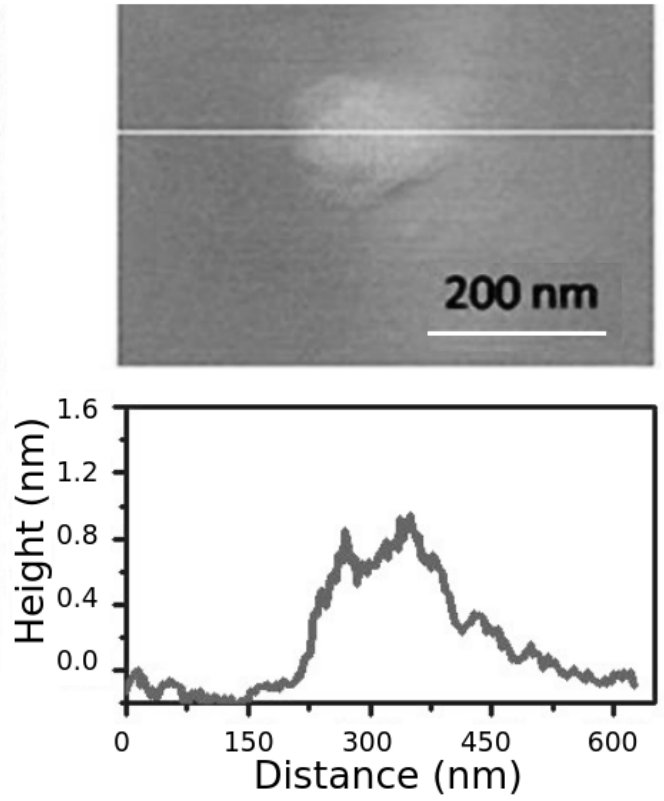

(b)

Figure 2.2: (a) Transmission electron microscopy and (b) atomic force microscopy of graphane (hydrogenated graphene). [8]

-COCl groups, followed by reaction with a long chain aliphatic–amine[2] to obtain the amide derivative soluble in nonpolar solvents [65]. Another method is by inserting aryl groups (which are a group of atoms derived from benzene or from a benzene derivative by removing one hydrogen that is bonded to the benzene ring) through diazotization reaction [66]. Soluble graphene layers in tetrahydrofuran can be generated by the covalent attachment of alkyl chains to graphene layers via reduction of graphite fluoride with alkyl lithium reagents [67]. Such covalent functionalization enables solubilization in organic solvents such as CCl_4, CH_2Cl_2 and THF [54].

The reaction of graphene with a mixture of concentrated H_2SO_4 and HNO_3 gives water–soluble graphene which is stable for several months. Graphene is solubilized in CCl_4 by interaction with organosilane, a kind of chemical compound that involves carbon and silicon, and organotin, which are chemical compounds based on tin with hydrocarbon substituents, and reagents such as hexadecyltrimethoxysilane and dibutyldimethoxytin [68].

Without making changes in the electronic structure, Graphene can be functionalized through non–covalent modification by enveloping with surfactants or through π–π interaction with aromatic molecules such as1–pyrenebutanoic acid succinimidyl ester (I) and thepotassium salt of coronene tetracarboxylic acid (II).

Interaction with molecules of the type II with few–layers graphene produce exfoliation and selectively solubilizing single and double–layer graphenes in water through molecular charge–transfer interaction [53]. Non–covalent interaction of graphene with surfactants such as compounds of type (polyoxyethylene nonylphenylether, IGP), sodium dodecylsulfate(SDS) and cetyltrimethylammoniumbromide (CTAB) gives water–soluble graphene. Water–soluble graphene can also be obtained by PEGylation method. In this method acidified graphene is treated with excess of polyethylene glycol -HCl under solvothermal conditions [54].

[2] An aliphatic–amine is an amine in the molecule of which there are no aromatic rings directly on the nitrogen atom.

2.3 Some Chemical and Electronical Properties of Graphene

The distinctive electronic, thermal and mechanical properties of graphene make it a very promising candidate for a wide range of applications in nanoscience and nanotechnology. The versatile properties of graphene are very well documented in the exponentially growing literature. Some of its interesting properties and its technological implications are discussed hereafter.

2.3.1 Electronic properties

The great potential to use graphene for electronics is due to the extraordinarily high mobility of its charge carriers at room temperature. Now when the Si–based technology is reaching its fundamental limits, graphene seems to be a possible answer to take over from silicon [1]. The band gap property in semiconductors has a central role in modern device physics. Moreover, it is a inherent property of semiconductors and insulators and determines their charge transport and optical properties [17]. An important discovery was that tere is possible to open and tune the band gap of graphene by applying an electric field [17] or by doping, like is shown in Fig. (2.3) [69]. According to these results graphene has the potential to be used in electronics. The structure of graphene can be modeled to change its electronic properties by several methods. Moreover, the structural manipulation of graphene can induce optical properties, like band–gap opening, and then resulting to have potential for opto–electronic applications. Some of these possibilities are discussed in the next subsection.

2.3.2 Interaction of graphene with other molecules

Raman bands of graphene are affected strongly by electron–phonon interactions and then by doping with holes and electrons. It has been found recently that a top–gated single layer graphene transistor is able to reach doping levels of up to $5 \times 1013\,\mathrm{cm}^{-1}$ by Raman spectroscopy measurements [70]. The G–band and 2D–band show changes when doping. Electron–donor and electron–acceptor molecules have been found to affect the Raman spectrum of few–layers graphene giving rise to rather large shifts in the Raman bands positions and band widths. The changes in the Raman spectrum done

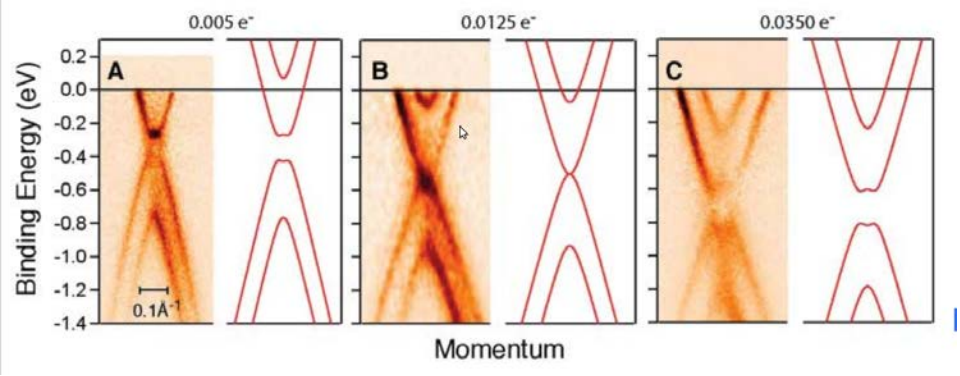

Figure 2.3: Evolution of gap closing and reopening by changing the doping level by potassium adsorption. Experimental and theoretical bands (solid lines) (A) for an as–prepared graphene bilayer and (B and C) with progressive adsorption of potassium.

due to the interaction of tetrathiafulavalene (TTF) and tetracyanoethylene (TCNE) with few–layers exfoliated graphene present [71], the shifts in the G–band going up to 25 cm^{-1}. A possibility for that changes in the Raman spectrum is considered to be due to surface effects. There has been investigated the effects of TTF and TCNE on the Raman bands using few–layers graphenes prepared by three different methods and then there has been associated with differences in the nature of the surface according to [72].

There has been followed the variation in the G–bands of EG, DG and HG changing the concentrations of TTF and TCNE. All the samples showed an increase in the G–band frequency when the interaction was with TCNE and a decrease in the G–band frequency when the interaction was with TTF. The changes in the G–band frequency becomes a maximum in the case of EG and least in HG. Thus, the shifts in the G–band in the EG, DG and HG samples are 25,17 and 11 cm^{-1} respectively on interaction with 0.1M TCNE. The full–width–at–half–maxima (FWHM) of the G–bands of the three graphene samples also vary with the concentration of TTF and TCNE. The FWHM of the G–band generally increases on interaction with TTF and TCNE, the magnitude of increase being highest in the case of EG. We also notice that the initial increase is generally sharp. We could obtain reliable data on the changes in the G' band in the case of HG. The FWHM of the G' band also increases with the increase in concentration of TTF or TCNE.

In Fig. 2.4 [44] the ratio of intensities of the of 2D and G bands, $I_{(2D)}$ /$I_{(G)}$

against the concentrations of TTF and TCNE. It is possible to see that the 2D–band intensity decreases with the increase of concentration of TTF and TCNE has been plotted ; the decrease in intensity is higher with EG and DG in comparison to HG. The intensity of the defect–related D band also varies with the TTF/TCNE concentration, but in an opposite direction to that of the 2D–band as depicted in Fig. 2.4b. This behavior is due to difference between the origin of the 2D and D bands: the D–band, unlike the 2D–band, couples to electronic states with the wave vector $\vec{k}$ such that $2q = k$ [73]. In the case of the D–band two scattering events are present: one is an elastic process involving defects and the other is inelastic involving. On the other hand, in the case of the 2D–band, both processes involving phonons are inelastic.

2.3.3 Properties of non covalent binds

The weak, intermolecular, Van der Waals' and $\pi - \pi$ interactions [74] have a crucial role in the crystal packing of organic molecules containing aromatic rings [75, 76]. Graphene sheets can be stacked into bilayers and multilayers due to the π–π interactions between the surrounding sheets. The electronic properties of multilayer graphene vary with the stacking order and evolve with the number of layers approaching the 3D limit of graphite [1, 77].

To make a theoretical model of weak Van der Waals' interaction in the conventional density functional theory is necessary to make an appropriate correction in the term for Van der Wals' interaction. With such a treatment, there have been shown that the stacked segments sheets of graphene can be held together in different orientations by $\pi - -\pi$ interactions and then the binding energy is dependent on the size of the polycyclic aromatic hydrocarbons, on the heaping order, and on the number of stacked layers [78]. The bi–layer graphene has some uncommon electronic properties like the anomalous integer quantum Hall effect which is different with respect to a single–layer graphene [79–81], and which can be used to discriminate between single–layered and bi–layered graphene. Moreover, the bi–layered graphene's band–gap is tunable in different ways [17, 69]. The importance of bilayer graphene emphasizes the importance to understand the binding between the two sheets. There has been shown in bilayer models that the binding energy increases with size until it saturates when the size of about 80 atoms is reached [78]. So, according to the studies of graphene mentioned before, understanding the weak Van der Wals' interactions is relevant to

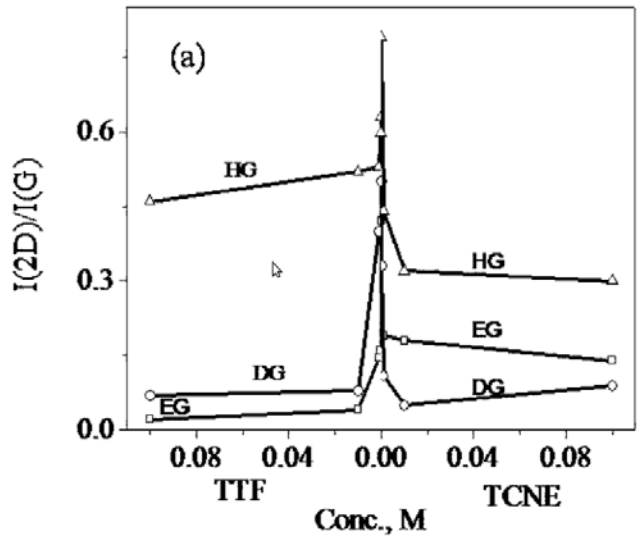

(a)

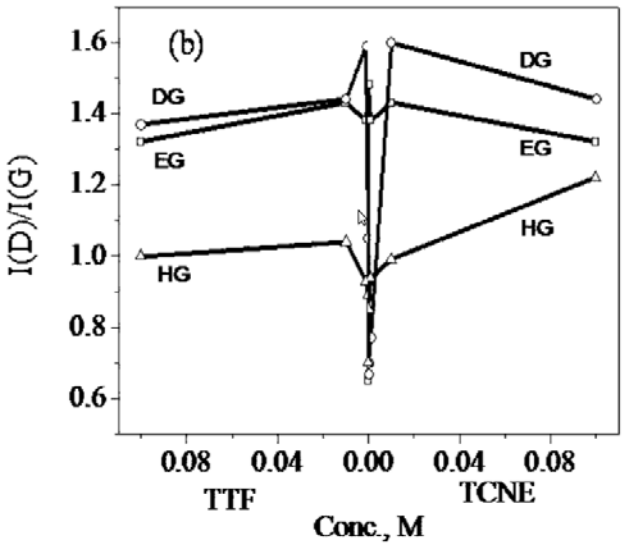

(b)

Figure 2.4: Variation in (a) 2D/G and (b) D/G intensity ratios with the concentration of TTF and TCNE [44]

have potential applications of graphene.

2.4 Optical Properties of Graphene and Graphane

The quantum phenomena of graphene manifiest when the π electrons are confined laterally e.g. in graphene segments [40, 78] or graphene nanoribbons [9]. The energy gap opens up when carriers are confined to a quasi–one dimensional system like in graphene nanoribbons. That kind of systems have optical properties which can change with their width, family, crystallographic orientation and edge termination [82, 83]; a similar behavior apears in carbon nanotubes. There has been found that the energy gap of lithographically patterned graphene nanoribbons scales inversely with the ribbon width. According to that, there exists the possibility to engineer the band gap of graphene nanostructures by lithographic processes [9]. Another possibility to induce the formation of a band gap is, as was mentioned before, by the hydrogenation of graphene [84–86]. The modification in the carbon bonds associated with the hydrogenation maintain the crystalline lattice but leads to rehybridization of the carbon atoms from a planar sp^2 to a distorted sp^3 state [87]. Recent experimental studies have shown that is possible to have a reversible hydrogenation through heating [84].

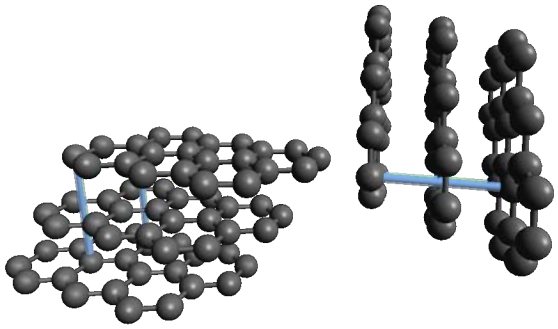

Figure 2.5: Arrange of carbon atoms in two adjacent planes in ABA stacking.

Previously it was mentioned that hydrogen plays an important role in luminescence. The bandwidth luminescence between 1.5 ev and 2.5 eV from carbon layer compounds has been attributed to the presence of a sp^2 amorphous phase or graphite phase [88, 89]. The distribution of states within the

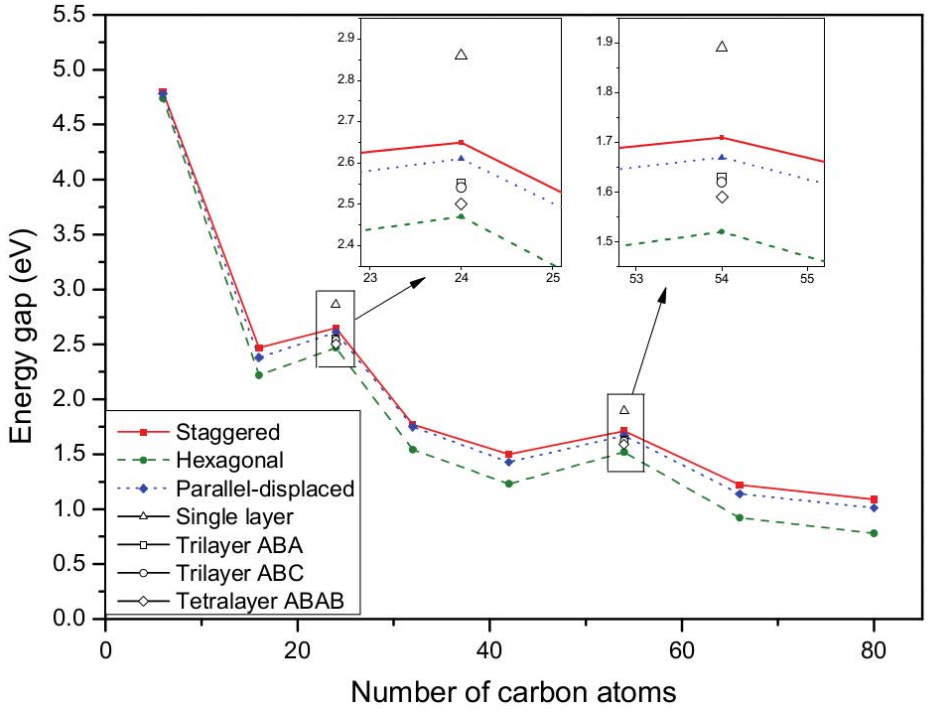

Figure 2.6: Variation of the energy gap with the size of graphene sheet model dimers for the staggered, hexagonal, and parallel–displaced stackings, respectively.

energy gap introduced by an sp^2 disordered phase in a nanodiamond film deposited by chemical vapor has been considered as the origin of the broadband luminescence [29], based on the theory of amorphous material. Furthermore, the process of luminescence and recombination in a C:H and its alloys has been suggested because of modifications of the band edges in hydrogenated amorphous silicon [90–92]. The band–tail states were assumed to come up from clusters of sp^2 sites. The π–bonding sp^2 phase has been associated to the origin of the luminescence [31, 32, 93]. The broadband luminescence is often assumed to be related to the gap/tail states produced from small sp^2 clusters with different sizes and/or shapes. A new photoluminescence model, taking account of individual clusters, has presented an overwhelming mechanism [94]. At the moment, clear pictures of which structures or shapes of sp^2 carbon clusters bring the highly efficient luminescence were lacking. In a diamond that is further a pure sp^3–bonded material, the gap is indirect and also wide: 5.49 eV at 77 K. The gap of a nano–structural diamond–like crystals may be larger, and so may not be related to the luminescence phenomena that is concerned in the range of $1.5 - 2.5\,eV$ produced by means of optical transitions between band states. Otherwise, the π–bonding states of graphite is near to the Fermi level, so apparently it is not possible to find the relationship between the gap formed by these states and the luminescence in the range of 1.5 and 2.5 eV. Nevertheless, a nano–sized π–bonding sp^2 cluster may show a wide energy gap when is compared with that of the graphite material, as has been shown in reference [40], which agrees with the size–dependence rule that holds for many other materials. This property has appeared in the calculations with a Hückel approximation for several sp^2 carbon clusters [95, 96]. Notwithstanding, all previous works was only qualitative and did not discriminate the different characteristics of states in the gap–tail due to the individual sp^2 carbon clusters caused by differences in sizes and/or shapes.

For the carbon–based materials mentioned before, like graphene, carbon nanoribbons and carbon nanotubes, has been shown that both, the size and shape, determine the energy gap and the broadband luminescence [90–92, 94]. However, any structural deviation from the "perfect stable" configurations (some of them shown in table 1.1) may produce localized states that can change the energy gap. As was mentioned in the previous paragraph, the energy gap of localized states do not relate to the efficiency, room temperature luminescence. Thus, the small clusters with structures such as a fivefold ring, sevenfold ring and off–lane hexagonal, that are not the stable hexagonal structures are doubtful of produce a contribution in the efficient

broadband luminescence. Instead that, the main source for such luminescence would be due to the stable hexagonal carbon clusters. According to calculations of a series of small hexagonal carbon clusters like those in Fig. 1.1, or a fraction of it, demonstrated that the energy–gap distribution, due to variations in size is substantially wide, which explains the broadband peculiarity of luminescence. The weak $\pi - \pi$ bond allows multilayer stacking of graphene sheets the and possible ways [78] depicted in Fig. 2.5 and so helps the generation of stable large–sized sp^2 C-H films. Some calculations show that the energy gaps of graphene are dependent on their sizes [78], whereas the stacking order and the amount of stacked sheets have less influence. There has been found that the energy gap decreases when the sheet size is increased, as shown in Fig. 2.5 [15]. The open symbols and the insets show the energy gaps of $C_{24}H_{12}$ and $C_{54}H_{18}$ monomers, and their trimers with ABA and ABC stackings, and tetramers with an ABAB sequence. So, by controlling the formation of graphene during a chemical vapor deposition, is possible to tune its luminescent properties.

2.5 Summary

In this introductory chapter it has been presented some important knowledge about graphene and graphane. There was described some process to obtain graphene, like chemical vapor deposition, starting from other substances or by mechanical methods. Also was explained the functionalization of this interesting compound along with some of the physical. In the following chapter some quantum, electric and optical properties will be presented. They will help to reach the central theme of interest in this work.

Chapter 3

Quantum Background Theory

Contents

The spin–orbit interaction is a quantum process in which the particle's spin interacts with its motion. The best known example of this phenomena, and the first studied, occurs when the spin–orbit interaction produces shifts in an electron atomic energy levels due to the electromagnetic interaction between the electron's spin and the magnetic field generated by the electron's orbiting around the nucleus that produces the splitting of spectral lines. An analogous effect, due to the connection between angular momentum and the strong nuclear force, occurs with protons and neutrons which are in movement inside the nucleus, producing a shift on their energy levels in

the nucleus shell model. In the research of spintronics, the intrinsic spin of electrons, the associated magnetic moment and the fundamental electronic charge, are the basis to study the spin–orbit effects in semiconductors and other materials.

Spintronics was developed from discoveries in the 1980s of spin–dependent electron transport phenomena in the study of solid–state devices. This includes the observation of spin polarization injection in electrons from a ferromagnetic metal to a normal metal [97] and the discovery of "giant magnetoresistance" effects over the expected order of magnitude [98]. The beginning of spintronics can be traced back to the ferromagnet/superconductor tunneling experiments and the first experiments on magnetic tunnel junctions [99] in the 1975. The development of spintronics in semiconductors initiated with the theoretical proposal of a spin field–effect–transistor [100] in 1990.

In some materials, called "dilute magnetic semiconductors" [101], such as GaMnAs and Si–3D [102] the spin current can be controlled by applying a gate voltage but spin injection and spin device operation at room temperature (RT) has not been achieved. Since graphene exhibits gate–voltage–controlled carrier conduction, virtual absence of nuclear magnetic moments and high field–effect mobilities and because it is constituted only by carbon atoms which have a low atomic mass that induces a small spin–orbit interaction, graphene has the potential to be a material for spintronics in which the polarized spin current can be controlled by a magnetic field, drain voltage and by a gate voltage [103].

In this chapter the knowledge needed about the quantum theory behind the spintronics and the process to study the optical spin injection will be presented.

3.1 Quantum Theoretical Basis

3.1.1 Quantum Spin Theory

In nature there exist two kinds of elemental particles, bosons and fermions. Bosons obey the Ferm–Dirac statistics which applies to identical particles with half–odd–integer spin in a system in thermal equilibrium, where the particles in the system are assumed to have negligible mutual interaction, allowing the many–particle system to be described in terms of single–particle

energy states. A system composed whit bosons does not obey the Pauli's exclusion principle and can be described by the Bose–Einstein statistics

$$n(\varepsilon) = \frac{1}{e^{(\varepsilon-\mu)/k_B T} - 1}\,, \tag{3.1}$$

where n_i is the number of particles in the state i, g_i is the degeneracy of state i, ε_i is the energy of the i^{th} state, μ is the chemical potential, k is the Boltzmann constant and T is the absolute temperature. If the conditions $\varepsilon_i > \mu$ and $kT >> \varepsilon_i - \mu$ are satisfied the Eq. (3.1) can be reduced to the Rayleigh–Jeans Law distribution

$$n_i(\varepsilon) = \frac{g_i kT}{\varepsilon_i - \mu}. \tag{3.2}$$

In contrast with bosons, fermions, which can be elementary particles like electrons, are particles with half–integer spin with intrinsic angular momentum $\hbar$ and are distinguished because only one particle can occupy a quantum state at any given time; if more than one fermion shares the same physical space, at least one property of each fermion, such as its spin, must be different. On the other hand, fermions are characterized by Fermi–Dirac statistics which establishes that for a system of identical fermions, the average number of fermions in a single–particle state i is

$$n(\varepsilon) = \frac{1}{e^{(\varepsilon-\mu)/kT} + 1}. \tag{3.3}$$

Also, fermions obey the Pauli exclusion principle and so the wave function of two identical fermions are anti–symmetric with respect to exchange of particles.

The "total angular momentum", $\hat{J}$, of a particle is the sum of the "extrinsic" angular momentum, $\hat{L}$, plus to the "intrinsic" angular momentum, $\hat{S}$,

$$\hat{J} = \hat{L} + \hat{S}. \tag{3.4}$$

The angular moment corresponds to the movement of electrons around the nuclei in specific zones called orbitals. The spherical harmonics, Y_ℓ^n, correspond to the solution to the Laplace's equation, $\nabla\varphi = 0$, in the spherical coordinated system and define the atomic orbital electron configurations where there is a probability of 99% of finding an electron in a defined region

of space. Some spherical harmonics, only for the values where $0 \leq n \leq 3$, and so, the corresponding given values to ℓ ($\ell = -n, \ldots, 0, \ldots, +n$) are depicted in Fig. 3.1 [104].

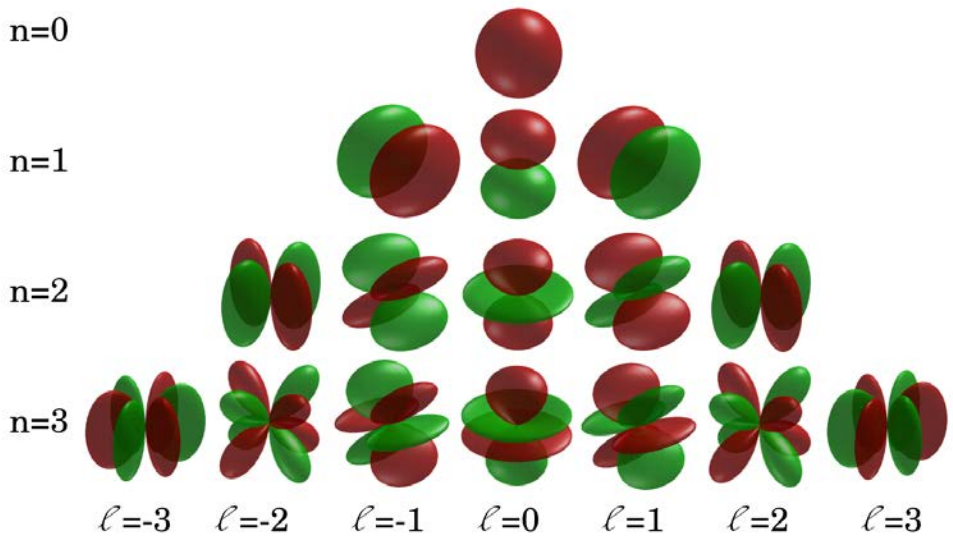

Figure 3.1: Spherical Harmonics corresponding to the values of $n = 0, 1, 2, 3$ and the corresponding values for ℓ ($-n, \ldots, 0, \ldots, +n$).

The idea about a rotational motion, or spin, of electrons was proposed in 1926 by George Uhlenbeck and Samuel Goudsmit [105] to explain the characteristic spectra in atoms which have only one electron. The existence of spin in electrons has been confirmed by many experimental results; the most important one was the Stern–Gerlach Experiment [106]. This experiment was similar to the Thomson's to determine the nature of cathodic rays. Both involves a beam of particles through a magnetic field to measure their deflection. If an inhomogeneous magnetic field is used then it is possible to avoid the large deflection due to the orbit of a charged particle. It allows spin–dependent effects to dominate.

According to the characteristics explained before the total angular momentum of the electron ($\hat{J}_e$), a structureless point particle, can be obtained by the sum of the orbital (angular momentum due to its orbital motion analogous to that around the nuclei) and spinorial contributions, as was mentioned in (3.4). It follows that the "algebraic" theory of spin orbital angular

momentum, starting with the fundamental commutation relations [107, 108]

$$[S_i, S_j] = i\hbar\varepsilon_{ijk}S_k\,; \qquad [S_i, S^2] = 0\,. \tag{3.5}$$

and then, the eigenvectors of S^2 and S_z satisfy

$$S^2|sm\rangle = \hbar^2 s(s+1)|sm\rangle; \qquad S_z|sm\rangle = \hbar m|sm\rangle, \tag{3.6}$$

and

$$S_\pm|sm\rangle = \hbar\sqrt{s(s+1) - m(m\pm 1)}|s(m\pm 1)\rangle\,, \tag{3.7}$$

where

$$S_\pm \equiv S_x \pm iS_y\,. \tag{3.8}$$

Because the eigenvectors are not Spherical Harmonics[1] there is no apriori reason to exclude the half–integer values of s and m [109] and then

$$s = 0, \frac{1}{2}, 1, \frac{3}{2}, \ldots \qquad m = -s, -s+1, \ldots, s-1, s. \tag{3.9}$$

Now, working with Eq. (3.8) we can obtain the expressions for the components of the spin operator, $\hat{\mathbb{S}}$, in terms of the Pauli spin matrices

$$\hat{\mathbb{S}} = \hat{s}^i = \frac{\hbar}{2}\hat{\sigma}^i\,, \tag{3.10}$$

from where $\hat{\sigma}^i$ represent the three Pauli matrixes

$$\hat{\sigma}^x = \begin{pmatrix} 0 & 1 \\ 1 & 0 \end{pmatrix}; \qquad \hat{\sigma}^y = \begin{pmatrix} 0 & -i \\ i & 0 \end{pmatrix}; \qquad \hat{\sigma}^z = \begin{pmatrix} 1 & 0 \\ 0 & -1 \end{pmatrix}. \tag{3.11}$$

3.2 Electrons embedded in magnetic fields

If an electron, or any other charged particle, is spinning then it will produce a magnetic field and so a magnetic dipole, $\boldsymbol{\mu}$, proportional to the intrinsic angular momentum or spin, $\boldsymbol{s}$,

[1] When we are solving the Schrödinger equation in spherical coordinates the "Spherical Harmonics" are the solution. Then we obtain the wave function $\Psi_{n\ell m}(r,\theta,\phi) = A_{n\ell}J_\ell(\beta_{n\ell}\,r/a)Y_\ell^m(\theta,\phi)$. The values of n, ℓ, and m are restricted to be integers.

$$\boldsymbol{\mu} = \gamma \boldsymbol{s}, \tag{3.12}$$

like is shown in Fig. 3.2. Here the proportionality constant, γ, is called the "gyromagnetic ratio" and is defined as

$$\gamma = -g_e \frac{\mu_B}{\hbar},$$

from where g_e is denominated the "electron spin g–factor" [110,111] and μ_B is the Bohr magneton

$$\mu_B = \frac{e\hbar}{2m_e}.$$

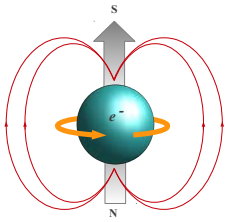

Figure 3.2: Magnetic dipole generated for a spinning particle.

Also the number of possible orientations of the angular momentum vector is $2s+1$. It follows that when a magnetic dipole is placed in a magnetic field, $\boldsymbol{B}$, a torque is produced tending to line up the dipole in a parallel direction to the field. The energy, E, associated with this effect is

$$E = -\boldsymbol{\mu} \cdot \boldsymbol{B}\,, \tag{3.13}$$

and so, the Hamiltonian of a spinning charged particle at rest placed in a magnetic field can be written as

$$\hat{H} = -\gamma \boldsymbol{s} \cdot \boldsymbol{B}\,, \tag{3.14}$$

where $\hat{\mathbb{S}}$ is given by the expressions shown in (3.10) and (3.11). Studying the case where the spin is $\frac{1}{2}$, which is the case when the third matrix of (3.11) is taken and which corresponds to the electron, then the Hamiltonian matrix can be written as

$$\hat{H} = -\gamma B_0 \hat{s}^z = -\gamma B_0 \frac{\hbar}{2} \begin{pmatrix} 1 & 0 \\ 0 & -1 \end{pmatrix}. \tag{3.15}$$

and so, the vectorial component along the fixed axis only have two possible values

$$s^z = +\tfrac{1}{2}\hbar, \tag{3.16}$$

and

$$s^z = -\tfrac{1}{2}\hbar\,. \tag{3.17}$$

These equations are called "spin up" and "spin down", respectively.

3.3 Density Functional Theory and Spin–Density Theory

In the formulation of the Density Functional Theory was shown that a special role can be assigned to the density of particles in the ground state of a quantum many–body system: the density can be considered as a "basic variable," and so, all properties of the system can be considered to be unique functionals of the ground state density.

The Density Functional Theory can be used to develop electronic structure calculations. Proposed by Walter Kohn and Lu Jeu Sham, they introduced the concept in 1965 to supersede the many–body problem to an auxiliar independent–particle problem, having "exact" calculations of many–body systems. The Kohn–Sham approach involves independent particles but an interacting density.

Using the Kohn–Sham approach it is possible to replace the difficult interacting many–body system obeying the hamiltonian to a different auxiliar system that can be solved in an easier way. Also, it is possible to assume that the ground state density of the original interacting system is equal to that of some chosen non–interacting system.The Kohn–Sham's mathematical development requires to assume that:

1. The exact ground state density can be represented by the ground state density of an auxiliary system of non–interacting particles.
2. The auxiliary hamiltonian is chosen to have the usual kinetic operator and the effective local potential $V_\sigma^{\mathrm{eff}(\boldsymbol{r})}$ acting on an electron of spin σ at point $\boldsymbol{r}$.

If an external magnetic field is applied to an electronic system, it generally couples both to the electron spin and to the electronic orbital current. A

framework for the description of spin coupling is provided by the "spin–density–functional theory". The variables of spin–density–functional theory are the scalar electronic density, $n(\boldsymbol{r})$, and the magnetization density vector, $\vec{m}(\boldsymbol{r})$. Then, the spin density matrix, $n_{\alpha\beta}(\boldsymbol{r})$, can be used where the indices α and β can have only the "values" + and − (also sometimes denoted as ↑ and ↓) that corresponds to the spin–up (3.16) and spin–down (3.17) equations, respectively. This variables can be written as

$$n(\boldsymbol{r}) = \sum_{\alpha} n_{\alpha\beta}(\boldsymbol{r}); \qquad \vec{m}(\boldsymbol{r}) = \sum_{\alpha\beta} = \vec{\sigma}_{\alpha\beta} n_{\alpha\beta}(\boldsymbol{r})\,, \tag{3.18}$$

where

$$n_{\alpha\beta}(\boldsymbol{r}) = \tfrac{1}{2} n(\boldsymbol{r})\delta_{\alpha\beta} \; + \; m_x(\boldsymbol{r})\sigma^{\,x}_{\alpha\beta} + m_y(\boldsymbol{r})\sigma^{\,y}_{\alpha\beta} + m_z(\boldsymbol{r})\sigma^{\,z}_{\alpha\beta}\,, \tag{3.19}$$

from where $\sigma^{x}_{\alpha\beta}$, $\sigma^{y}_{\alpha\beta}$ and $\sigma^{z}_{\alpha\beta}$ are the Pauli spin matrices given in Eq. (3.11).

The Hohemberg–Kon–Sham spin–density functional [112, 113] is given by

$$\begin{aligned} E[n_{\alpha\beta}(\boldsymbol{r})] = \quad & T_s[n_{\alpha\beta}(\boldsymbol{r})] \; + \; \tfrac{e^2}{2} \iint \frac{n(\boldsymbol{r})\, n(\boldsymbol{r}')}{|\boldsymbol{r} - \boldsymbol{r}'|}\, \mathrm{d}\boldsymbol{r}\, \mathrm{d}\boldsymbol{r}' \\ & + \sum_{\alpha\beta} \int V^{\,\mathrm{ext}}_{\alpha\beta}(\boldsymbol{r})\, n_{\alpha\beta}(\boldsymbol{r})\, \mathrm{d}\boldsymbol{r} + E_{xc}[n_{\alpha\beta}(\boldsymbol{r})]\,, \end{aligned} \tag{3.20}$$

as a sum of the kinetic energy, T_s, of non–interacting electrons, the electron–electron interaction in the Hartree approximation, the interaction energy with the external potential, $V^{\,\mathrm{ext}}_{\alpha\beta}$, and the exchange–correlation energy, $E_{xc}[n_{\alpha\beta}(\boldsymbol{r})]$.

Using the single–particle wavefunctions (orbitals) $\varphi^{i}_{\alpha}(\boldsymbol{r})$ [114] the kinetic energy functional, $T_s[n_{\alpha\beta}(\boldsymbol{r})]$, and the spin–density matrix, $n_{\alpha\beta}(\boldsymbol{r})$, it is possible to write the kinetic energy functional as

$$T_s[n_{\alpha\beta}(\boldsymbol{r})] = \sum_{\alpha i} \int \varphi^{i*}_{\alpha}(\boldsymbol{r}) \left(-\frac{\hbar^2}{2m} \nabla^2_{\boldsymbol{r}}\, \varphi^{i}_{\alpha}(\boldsymbol{r}) \right) \mathrm{d}r\,, \tag{3.21}$$

and the spin density matrix as

$$n_{\alpha\beta}(\boldsymbol{r}) = \sum_{i} \varphi^{i*}_{\alpha}(\boldsymbol{r}) \varphi^{i}_{\beta}(\boldsymbol{r})\,, \tag{3.22}$$

where the sum over i includes all occupied orbitals. The Eqs. (3.21) and (3.22) give an implicit representation of the kinetic energy in terms of the

spin–density matrix. Also, in terms of the "spin up" and "spin down" orbitals, denoted respectively as $\varphi^i_+(\boldsymbol{r})$ and $\varphi^i_-(\boldsymbol{r})$, the corresponding spin densities can be represented as

$$n_\pm(\boldsymbol{r}) = \sum_i |\varphi^i_\pm(\boldsymbol{r})|^2 \,. \tag{3.23}$$

The Kohn–Sham equations provide a modification to the Schrödinger equation in order to describe a system of non interacting electrons that generates the same electron density as any given system of interacting particles [115]. In a local effective potential, $V^{\text{eff}}_\pm$, the Kohn–Sham equation for the orbitals can be written as

$$\left(-\frac{\hbar^2}{2m}\nabla^2_{(\boldsymbol{r})} + V^{\text{eff}}_\pm(\boldsymbol{r})\right)\varphi^i_\pm(\boldsymbol{r}) = \epsilon_{i_\pm}\varphi^i_\pm(\boldsymbol{r})\,, \tag{3.24}$$

with an effective potential given by

$$V^{\text{eff}}_\pm(\boldsymbol{r}) = e^2\int \frac{n(\boldsymbol{r}')}{|\boldsymbol{r}-\boldsymbol{r}'|}\,\mathrm{d}\boldsymbol{r}' + V^{\text{ext}}_\pm(\boldsymbol{r}) + V^{\text{xc}}_\pm(\boldsymbol{r})\,. \tag{3.25}$$

In Eq. (3.25) let us consider the case when an external magnetic field, H, is applied and so, the external potential, $V^{\text{ext}}_\pm$ contains a field term $-(\pm\mu_B H$ where the minus sign indicates that most of the spin–up electrons are energetically favored in comparison with the spin–down electrons. Also, the correlation potential

$$V^{\text{xc}}_\pm(\boldsymbol{r}) = \frac{\delta E^{\text{xc}}[n_+(\boldsymbol{r}), n_-(\boldsymbol{r})]}{\delta n_\pm(\boldsymbol{r})}\,, \tag{3.26}$$

is defined by the functional derivative of the exchange correlation energy and can have different values for the two possible spin directions even without an external magnetic field applied.

3.4 Determination of electronic structure

The method of expansion in plane waves provides the methodology to solve differential equations, including the Schrödinger's equation. This methodology plus the Bloch's theorem is specially appropriate for periodic systems providing intuitive understanding algorithms for practical calculations.

3.4.1 The independent–particle Schrödinger–like equation in a plane wave basis

The eigenstates of any independent particle Schrödinger–like equation in which each electron moves in an effective potential $V^{\text{eff}}(\boldsymbol{r})$, satisfy the eigenvalue problem given in Eq. (3.24). In the study of condensed matter is conveniently required that the states be normalized and obey periodic boundary conditions in the volume Ω of an unit cell. Using the fact that any periodic function can be expanded in complete set of Fourier components, an eigenfunction can be writen as

$$\varphi^i(\boldsymbol{r}) = \sum_{\boldsymbol{q}} c_{i,\boldsymbol{q}} \frac{1}{\sqrt{\Omega}} \exp(i\boldsymbol{q}\cdot\boldsymbol{r}) \equiv \sum_{\boldsymbol{q}} c_{i,\boldsymbol{q}} |\boldsymbol{q}\rangle \,, \tag{3.27}$$

where $c_{i,\boldsymbol{q}}$ are the expansion coefficients of the wavefunction in the basis of the orthonormal plane waves $|\boldsymbol{q}\rangle$ satisfying

$$\langle \boldsymbol{q}' |\, \boldsymbol{q}\rangle \equiv \frac{1}{\Omega} \int_{\Omega} \mathrm{d}\boldsymbol{r} \exp(-i\boldsymbol{q}\cdot\boldsymbol{r}) = \delta_{\boldsymbol{q},\boldsymbol{q}'} \,. \tag{3.28}$$

To obtain the Schrödinger equation in the Fourier space we need to substitute Eq. (3.27) in Eq. (3.24), multiply from the left by $\langle \boldsymbol{q}'|$ and integrate as has been done in Eq. (3.28) to obtain

$$\sum_{\boldsymbol{q}} \langle \boldsymbol{q}'|\hat{H}^{\text{eff}}|\boldsymbol{q}\rangle c_{i,\boldsymbol{q}} = \varepsilon_i \sum_{\boldsymbol{q}} \langle \boldsymbol{q}' |\, \boldsymbol{q}\rangle \, c_{i,\boldsymbol{q}} = \varepsilon_i c_{i,\boldsymbol{q}'} \,. \tag{3.29}$$

Now we have that the matrix elements of the kinetic energy operator are given by

$$\langle \boldsymbol{q}'| -\frac{\hbar^2}{2m_e}\nabla^2 |\boldsymbol{q}\rangle = \frac{\hbar^2}{2m_e}|\boldsymbol{q}|^2 \delta_{\boldsymbol{q},\boldsymbol{q}'} \,. \tag{3.30}$$

If we have an anisotropic system, the potential $V^{\text{eff}}(\boldsymbol{r})$ is periodic and can be expressed as a sum of Fourier components

$$V^{\text{eff}}(\boldsymbol{r}) = \sum_{m} V^{\text{eff}}(\boldsymbol{G}_m) \exp(i\boldsymbol{G}_m\cdot\boldsymbol{r}) \,, \tag{3.31}$$

where $\boldsymbol{G}_m$ are the reciprocal lattice vectors and

$$V^{\text{eff}}(\boldsymbol{G}) = \frac{1}{\Omega_{\text{cell}}} \int_{\Omega_{\text{cell}}} \mathrm{d}\boldsymbol{r}\, V^{\text{eff}}(\boldsymbol{r}) \exp(-i\boldsymbol{G}\cdot\boldsymbol{r}) \,, \tag{3.32}$$

with Ω_{cell} defined as the volume of the primitive cell. Then we have that the matrix elements of the potential

$$\langle \boldsymbol{q}'|V^{\text{eff}}|\boldsymbol{q}\rangle = \sum_m (\boldsymbol{G}_m)\delta_{\boldsymbol{q}'-\boldsymbol{q},\boldsymbol{G}_m}\,, \tag{3.33}$$

are different from zero only if $\boldsymbol{q}$ and $\boldsymbol{q}'$ differ by some reciprocal lattice vector $\boldsymbol{G}_m$.

Now, defining $\boldsymbol{q} = \boldsymbol{k}+\boldsymbol{G}_m$ and $\boldsymbol{q}' = \boldsymbol{k}+\boldsymbol{G}_{m'}$, then the Schrödinger equation for any given $\boldsymbol{k}$ can be written as the matrix equation

$$\sum_{m'} H_{m,m'}(\boldsymbol{k})c_{i,m'}(\boldsymbol{k}) = e_i(\boldsymbol{k})c_{i,m}(\boldsymbol{k})\,, \tag{3.34}$$

where

$$\begin{aligned} H_{m,m'}(\boldsymbol{k}) = &\ \langle \boldsymbol{k}+\boldsymbol{G}_m|\hat{H}^{\text{eff}}|\boldsymbol{k}+\boldsymbol{G}_{m'}\rangle \\ = &\ \frac{\hbar^2}{2m_e}|\boldsymbol{k}+\boldsymbol{G}_m|^2\delta_{m,m'} + V^{\text{eff}}(\boldsymbol{G}_m-\boldsymbol{G}_{m'}). \end{aligned} \tag{3.35}$$

Eqs. (3.34) and (3.35) are the basic Schrödinger equations in a periodic crystal, leading to the formal properties of bands; to explain it the Bloch theorem is needed.

3.4.2 The Bloch's theorem and electron bands

The Bloch theorem.

All eigenfunctions of the Schrödinger equation [Eq. (3.34)], for a given value of $\boldsymbol{k}$ are given by Eq. (3.27) with the sum over $\boldsymbol{q}$ restricted to the values $\boldsymbol{q} = \boldsymbol{k}+\boldsymbol{G}_m$ which can then be written as

$$\begin{aligned} \varphi^{i,\boldsymbol{k}}(\boldsymbol{r}) = &\ \sum_m c_{i,m}(\boldsymbol{k}) \times \frac{1}{\sqrt{\Omega}}\exp[i(\boldsymbol{k}+\boldsymbol{G}_m)\cdot\boldsymbol{r}] \\ = &\ \exp(i\boldsymbol{k}\cdot\boldsymbol{r})\tfrac{1}{\sqrt{N_{\text{cell}}}}\,u_{i,\boldsymbol{k}}(\boldsymbol{r})\,, \end{aligned} \tag{3.36}$$

where $\Omega = N_{\text{cell}}$ and

$$u_{i,\boldsymbol{k}} = \frac{1}{\sqrt{\Omega_{\text{cell}}}}\sum_m c_{i,m}(\boldsymbol{k})\exp(i\boldsymbol{G}_m\cdot\boldsymbol{r})\,, \tag{3.37}$$

which has the periodicity of the media having an eigenvector of a product of $exp(\mathrm{i}\boldsymbol{k}\cdot\boldsymbol{r})$, a periodic function. Is required $\varphi^{i,\boldsymbol{k}}(\boldsymbol{r})$ to be orthonormal over

all the volume Ω; then the terms $u_{i,\boldsymbol{k}}(\boldsymbol{r})$ are orthonormal in the primitive cell, so

$$\frac{1}{\Omega_{\text{cell}}}\int_{\text{cell}} \mathrm{d}\boldsymbol{r}\, u^*_{i,\boldsymbol{k}}(\boldsymbol{r})u_{i',\boldsymbol{k}}(\boldsymbol{r}) = \sum_m c^*_{i,m}(\boldsymbol{k})c_{i',m}(\boldsymbol{k}) = \delta_{i,i'}\,. \tag{3.38}$$

This equation means that the coefficients $c_{i,m}(\boldsymbol{k})$ are orthonormal vectors in the discrete index m of the reciprocal lattice vectors.

Bands of eigenvalues and the Brillouin zone.

The first Brillouin zone is defined as the unit cell in the reciprocal space. The boundaries of this cell are given by planes related to points on the reciprocal lattice as is depicted in Fig. 3.3. It is found by the method of Wigner–Seitz in the Bravais lattice [116]. Determining the first Brillouin zone is necessary to describe the propagation of waves in a periodic medium

$$\begin{aligned} &E^{\text{total}}\left[V^{\text{eff}}\right] = \\ &\frac{1}{N_k}\sum_{\boldsymbol{k},i} w_{\boldsymbol{k},i}\left\{\sum_{m,m'} c^*_{i,m}(\boldsymbol{k})\left[\frac{\hbar^2}{2m_e}|\boldsymbol{K}_m|^2\delta_{m,m'} + V^{\text{ext}}(\boldsymbol{K}_m,\boldsymbol{K}_{m'})\right]c_{i,m'}(\boldsymbol{k})\right\} \\ &+\sum_{\boldsymbol{G}}\epsilon_{xc}(\boldsymbol{G})n(\boldsymbol{G}) + \frac{1}{2}4\pi e^2\sum_{\boldsymbol{G}\neq 0}\frac{n(\boldsymbol{G})^2}{G^2} + \gamma_{\text{Ewald}} + \left(\sum_\kappa \alpha_\kappa\right)\frac{N_e}{\Omega}\,. \end{aligned} \tag{3.39}$$

Since E^{total} is the total energy per cell, the average over $\boldsymbol{k}$ and the sum over band is in the same form for the calculation [117]

$$n(\boldsymbol{r}) = \frac{1}{N_k}\sum_{\boldsymbol{k},i} f(\varepsilon_{i,\boldsymbol{k}})n_{i,\boldsymbol{k}}(\boldsymbol{r})\,, \qquad \text{with} \quad n_{i,\boldsymbol{k}}(\boldsymbol{r}) = |\psi_{i,\boldsymbol{k}}(\boldsymbol{r})|^2\,. \tag{3.40}$$

Because the Schrödinger Eq. (3.34), is defined for each $\boldsymbol{k}$ separately, each state can be labeled by the wave vector $\boldsymbol{k}$. The eigenvalues and eigenvectors for each $\boldsymbol{k}$ are independent unless they differ by a reciprocal lattice vector.

In the limit of large volume Ω, the $\boldsymbol{k}$ points become a dense and continuum and the eigenvalues $\varepsilon_i(\boldsymbol{k})$ tend to group in continuous *bands*. At each $\boldsymbol{k}$ there are a discrete set of eigenstates labeled ($i = 1, 2, \ldots$) that may be found

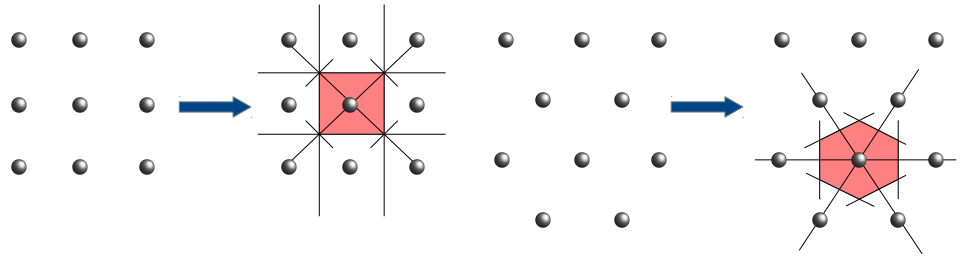

(a) Square lattice.

(b) Hexagonal honeycomb lattice corresponding to the graphene and graphane.

Figure 3.3: The reciprocal latices (dots) and the corresponding first Brillouin zones (red area) for two different lattices.

by diagonalizing the Hamiltonian, (3.35), in the basis of discrete Fourier components $\boldsymbol{k} + \boldsymbol{G}_m$, with $m = 1, 2, \ldots$

Since all possible eigenstates are specified by the wave vector $\boldsymbol{k}$ within the primitive cell of the periodic lattice in reciprocal space there is needed to define the concept of the Brillouin zone. The "first Brillouin zone" is the uniquely defined cell that is the most compact possible cell to represent excitations. It is unique among all primitive cell because its boundaries are the bisecting planes of the $\boldsymbol{G}$ vectors where Bragg scattering occurs [117]. Inside the Brillouin zone there are no boundaries: the bands must be continuous and analytic inside this zone. In Fig. (3.4) are shown the band structure of graphene [118, 119].

3.4.3 The empirical pseudopotential method

The actual model of pseudopotentials was developed by Phillips and Kleinman [120]. They found that the band structure of sp–bonded metals and semiconductors could be described by the values of the spherical atomic–like potentials at few lowest reciprocal lattice vectors. They also found that by using the empirical pseudopotential method and by fitting it to experimental data, a few parameters could be used to describe a large amount of data related to the bands structure, effective masses and band gaps, optical properties, etc. Using this method is also possible to describe the band structure

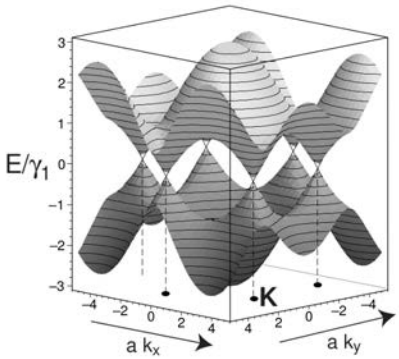

(a) 3D Band structure [118].

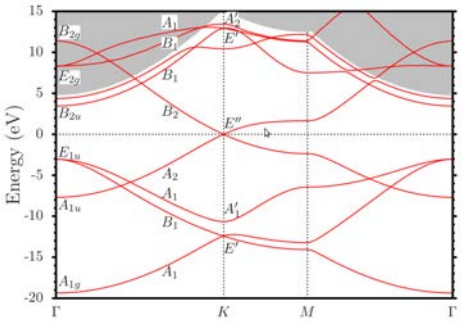

(b) Graphene band structure evaluation with use of FP–LAPW method [119].

Figure 3.4: In figure (a) is depicted the 3D band structure corresponding to a graphene honeycomb cell. In figure (b) the red–marked lines are well–converged single–layered graphene bands while gray background corresponds to continuous spectrum.

of materials using only few parameters, namely the "first few Fourier terms" of the potential

3.5 Full calculations using plane waves

The "Orthogonalized Plane Wave" method described in previous section is appropriate in cases where the potentials and wavefunctions are smooth. The additional required steps to complete a full self–consistent *ab initio*[2] calculation are:

1. If the calculation is "from first principles" then the pseudopotential must be derived from theoretical calculations. Such pseudopotentials are "bare potentials" and the total potential is determined.

2. The total effective potential in the Kohn–Sham Schrödinger–like equations is a sum of the bare ion pseudopotentials and the effective potentials from the valence electrons, the Hartree, and the exchange–

[2]The "*ab initio*" term comes from the Latin and means "from first principles". This term is widely used in literature of solid state physics. Furthermore, in this work is the term is used because both of the software projects used to make the calculations in this work, called "ABINIT" and "TINIBA", took them names from it.

correlation potential. This requires that the equations be solved in the self–consistence way.

3. The primary results in a Kohn–Sham density functional theory are the total energy and related quantities such as forces and stresses, which are sufficient for ground state properties. In addition, there are eigenvalues and eigenvectors that are only approximately related to the true excitation energies.

3.5.1 *Ab initio* pseudopotential method

The variational expressions for energy in terms of the output wavefunctions and density can be written [121–124]

$$E^{\text{total}}\left[V^{\text{eff}}\right] = \frac{1}{N_k}\sum_{\boldsymbol{k},i} w_{\boldsymbol{k},i}\left\{\sum_{m,m'} c^*_{i,m}(\boldsymbol{k})\left[\frac{\hbar^2}{2m_e}|\boldsymbol{K}_m|^2\delta_{m,m'} + V^{\text{ext}}(\boldsymbol{K}_m,\boldsymbol{K}_{m'})\right]c_{i,m'}(\boldsymbol{k})\right\} + \sum_{\boldsymbol{G}}\epsilon_{xc}(\boldsymbol{G})n(\boldsymbol{G}) + \frac{1}{2}4\pi e^2\sum_{\boldsymbol{G}\neq 0}\frac{n(\boldsymbol{G})^2}{G^2} + \gamma_{\text{Ewald}} + \left(\sum_{\kappa}\alpha_\kappa\right)\frac{N_e}{\Omega}\,. \tag{3.41}$$

Since E^{total} is the total energy per cell, the average over $\boldsymbol{k}$ and the sum over a band is in the same form for the calculation of [117]

$$n(\boldsymbol{r}) = \frac{1}{N_k}\sum_{\boldsymbol{k},i} f(\varepsilon_{i,\boldsymbol{k}})n_{i,\boldsymbol{k}}(\boldsymbol{r})\,, \qquad \text{with} \quad n_{i,\boldsymbol{k}}(\boldsymbol{r}) = |\psi_{i,\boldsymbol{k}}(\boldsymbol{r})|^2\,. \tag{3.42}$$

The sums, like those considered in reference [117], can be reduced to the "irreducible Brillouin zone". The potential terms involve $\boldsymbol{K} \equiv \boldsymbol{k} + \boldsymbol{G}_m$; the "xc" term is the total exchange–correlation energy. The expression given in Eq. (3.41) is a functional of V^{eff} which determines each term, except the final two that depend only upon the structure and number of electrons [117].

To make a proper treatment of the Coulomb terms is necessary to separate out the $\boldsymbol{G} = 0$ components in the potential and the total energy. The Hartree term in Eq. 83.41) describes the Coulomb repulsion interaction of electrons, except the divergent term due to the average electron density. Similary, the $\boldsymbol{G} = 0$ Fourier component of the local potential is defined to

be zero in Eq. (3.41). This last two terms mentioned before are included in the Ewald term[3], γ_{Ewald}, which is the energy of point ion in a compensating background containing the ion–ion terms as well as the interactions of the average electron density with the ions and with itself. The final term in Eq. (3.41) is a contribution due to the non–Coulombic part of the local pseudopotential where N_e/Ω is the average electron density, and α_κ is defined as

$$\alpha_\kappa = \int 4\pi r^2 dr \left[V_\kappa^{\text{local}}(r) - \left(-\frac{Z_\kappa}{r} \right) \right] . \tag{3.43}$$

Following the analysis made in reference [117] it is possible to define a functional

$$\begin{aligned} \widetilde{E} = \; & \frac{1}{N_k} \sum_{\boldsymbol{k},i} w_{k,i} \epsilon_i + \sum_{\boldsymbol{G}} \left[\varepsilon_{xc}(\boldsymbol{G}) - V_{xc}(\boldsymbol{G}) \right] n(\boldsymbol{G}) \\ & + \left[\gamma_{\text{Ewald}} - \frac{1}{2} 4\pi e^2 \sum_{G \neq 0} \frac{n(\boldsymbol{G})^2}{G^2} \right] + \left(\sum_\kappa \alpha_\kappa \right) \frac{N_e}{\Omega} , \end{aligned} \tag{3.44}$$

where all terms involve the input density $n \equiv n^{\text{in}}$. This last expression, Eq. (3.44), is very stable because it often converges faster to the final consistent energy, so that it is useful at every step of a self consistent calculation.

The force on any atom $\tau_{\kappa,j}$ can be found straightforwardly from the "force theorem" or "Hellmann–Feyman theorem" of reference [117] and so, from Eq. (3.41) we can obtain

$$\begin{aligned} \boldsymbol{F}_\kappa^j = -\frac{\partial E}{\partial \tau_{\kappa,j}} = \; & -\frac{\partial \gamma_{\text{Ewald}}}{\partial \tau_{\kappa,j}} - i \sum_m \boldsymbol{G}_m e^{i\boldsymbol{G}_m \cdot \tau_{\kappa,j}} V_\kappa^{\text{local}}(\boldsymbol{G}_m) n(\boldsymbol{G}_m) \\ & \times \; \frac{-i}{N_\kappa} \sum_{\boldsymbol{k},i} w_{k,i} \sum_{m,m'} c_{i,m}^*(\boldsymbol{k}) \Big[\boldsymbol{K}_{m,m'} e^{i(\boldsymbol{K}_{m,m'} \cdot \tau_{\kappa,j})} \\ & \times \; \delta V_\kappa^{\text{NL}}(\boldsymbol{K}_m, \boldsymbol{K}_{m'}) \Big] c_{i,m}(\boldsymbol{k}) , \end{aligned} \tag{3.45}$$

where the Ewald contribution can be found in appendix (F.10) of [117]. Then, the external pseudopotential has been separated into the local part, witch contains the long–range terms, and the short–range non–local operator $\delta V_\kappa^{\mathbf{ext}}(\boldsymbol{K}_m, \boldsymbol{K}_{m'})$, with $\boldsymbol{K}_{m,m'} = \boldsymbol{K}_m - \boldsymbol{K}_{m'}$.

[3] The Ewald sum [125] is the best technique for calculating electrostatic interactions in a periodic (or pseudo–periodic) system.

3.5.2 Solution to the Kohn–Sham equations

The Kohn–Sham equations, shown in Eqs. (3.34) and (3.35) with the local and non–local parts of the pseudopotential. Then, the local part of the potential can be written straightforwardly as the Fourier transform of the external local potential, Hertree, and "xc" potentials [117]. The first one, corresponding to the Fourier transform, can be expressed as

$$\begin{aligned} V(\boldsymbol{G}) &\equiv \frac{1}{\Omega_{\text{cell}}} \int_{\Omega_{\text{cell}}} V(\boldsymbol{r}) \exp(i\boldsymbol{G}\cdot\boldsymbol{r})\, \mathrm{d}\boldsymbol{r}\,, \\ &= \sum_{\kappa=1}^{n_{\text{species}}} \frac{\Omega_\kappa}{\Omega_{\text{cell}}} S_\kappa(\boldsymbol{G}) V_\kappa(\boldsymbol{G})\,, \end{aligned} \tag{3.46}$$

where the structure factor for each specie κ is

$$S_\kappa(\boldsymbol{G}) = \sum_{j=1}^{n^k} \exp(i\boldsymbol{G}\cdot\tau_{\kappa,j})\,, \tag{3.47}$$

and the form factor is

$$V_\kappa(\boldsymbol{G}) = \frac{i}{\Omega_\kappa} \int_{\text{all space}} V_\kappa(\boldsymbol{r}) \exp(i\boldsymbol{G}\cdot\boldsymbol{r})\, \mathrm{d}\boldsymbol{r}\,. \tag{3.48}$$

Also, the "xc" potential is given by

$$V_\sigma^{KS} = V^{\text{ext}}(\boldsymbol{r}) + V_{\text{Hartree}}(\boldsymbol{r}) + V_\sigma^{\text{xc}}(\boldsymbol{r})\,. \tag{3.49}$$

Then we have that

$$V_\sigma^{KS,\text{local}}(\boldsymbol{G}) = V^{\text{local}}(\boldsymbol{G}) + V_{\text{Hartree}}(\boldsymbol{G}) + V_\sigma^{\text{xc}}(\boldsymbol{G})\,, \tag{3.50}$$

where all $\boldsymbol{G} = 0$ Fourier components are omitted. They represent the average potential which is only a shift in the zero of energy. This has no consequence for the bands because the zero of energy is arbitrary in an infinite lattice.

Then, the full potential is the sum of Eq. (3.50) plus the non–local potentials [117]

$$\delta V_\kappa^{NL}(\boldsymbol{K}_m, \boldsymbol{K}m') = \sum_{lm_l} \frac{Y_{lm_l}(\hat{\boldsymbol{K}}_m) T_l^*(|\boldsymbol{K}_m|) \times T_l(|\boldsymbol{K}_{m'}|) Y_{lm_l}(\hat{\boldsymbol{K}}_{m'})}{\langle \psi_{lm}^{PS} | \delta V_l | \psi_{lm}^{PS} \rangle}\,. \tag{3.51}$$

The equations are solved by the self–consistent cycle shown in Fig. 3.5 where is shown an schematic representation of the self–consistent loop needed to find the solution to the Kohn–Sham equations. In general, one must iterate two such loops simultaneously for the two spins, with the potential for each spin a functional of the density of both spins.

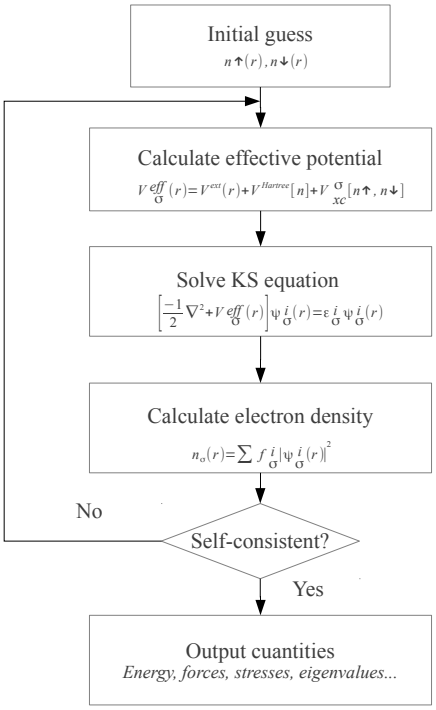

Figure 3.5: Schematic representation of the self–consistent loop for solution of Kohn–Sham equations.

The solution for a fixed potential is the same as for the non–self–consistent calculation; it is necessary to add just some more steps:

1. Calculation of the output density $n^{\text{out}}(\boldsymbol{G})$.

2. Generation of a new input density, $n^{\text{in}}(\boldsymbol{G})$, which leads to the new effective potential.

3. After self–consistency is reached, calculation of the total energy or related variational formulas.

3.5.3 Approach to self–consistency

The simplest approach is linear mixing

$$V_{\sigma,\mathrm{in}}(\boldsymbol{G}) = \alpha V^{i}_{\sigma,\mathrm{out}}(\boldsymbol{G}) + (1-\alpha)V_{\sigma,\mathrm{in}}(\boldsymbol{G})\,. \tag{3.52}$$

Choice of α by a trial–and–error process is often sufficient since the same value will apply to many similar systems.

In order to go further and analyse the convergence, one can treat the region near of convergence where the error in the output density or potentials is proportional to the error in the input potential δV_{in}.

The error in the output density $\delta V_{\mathrm{out}}(\boldsymbol{G}) = \delta V_{\mathrm{out}}(\boldsymbol{G})(G^2/4\pi e^2)$ is also governed by the dielectric function, and the kernel $\chi(\boldsymbol{G},\boldsymbol{G'}) = \epsilon(\boldsymbol{G},\boldsymbol{G'})G'^2/G^2$. In general, the dielectric function approaches to the large $\boldsymbol{G}$ or $\boldsymbol{G'}$.

3.6 Degree of spin polarization

Using the density matrix formalism [107], the expectation value of an observable, $\mathcal{O}$, is given by

$$\mathcal{O} = Tr\,(\hat{\rho}\,\hat{o})\ , \tag{3.53}$$

where Tr denotes the trace, given by the sum over the diagonal matrix elements, and $\hat{o}$ is the operator associated to the corresponding observable $\mathcal{O}$.

Now, using the closure relationship $\sum_c |c\boldsymbol{k}\rangle\langle c\boldsymbol{k}| = 1$ it is possible to write [126]

$$\begin{aligned}\mathcal{O} &= \int \frac{\mathrm{d}^3k}{8\pi^3}\sum_c \langle c\boldsymbol{k}|\hat{\rho}\,\hat{o}|c\boldsymbol{k}\rangle = \int \frac{\mathrm{d}^3k}{8\pi^3}\sum_{c,c'}\langle c\boldsymbol{k}|\hat{\rho}\,|c'\boldsymbol{k}\rangle\langle c'\boldsymbol{k}|\hat{o}|c\boldsymbol{k}\rangle\,,\\ &= \int \frac{\mathrm{d}^3k}{8\pi^3}\sum_{c,c'}(\boldsymbol{k})\rho_{c,c'}\mathcal{O}_{c',c}(\boldsymbol{k})\,.\end{aligned} \tag{3.54}$$

And now, using the so called relation "interaction picture"

$$\widetilde{\mathcal{O}}_{c'c} = \langle c'\boldsymbol{k}|e^{\mathrm{i}\hat{H}_0 t/\hbar}\,\hat{o}e^{-\mathrm{i}\hat{H}_0 t/\hbar}|c\boldsymbol{k}\rangle = \mathcal{O}_{c',c}\,e^{-\mathrm{i}\omega_{cc'}t}\,, \tag{3.55}$$

is then possible to write

$$\mathcal{O} = \int \frac{\mathrm{d}^3}{8\pi^3} \sum \widetilde{\rho}_{c\,c'}(\boldsymbol{k}) \tilde{\mathcal{O}}_{c'c}(\boldsymbol{k}) \,, \tag{3.56}$$

that will help to calculate the expectation value of the operator using $\hat{\rho}$ and $\hat{\mathcal{O}}$ in the Schrödinger representation. Then is possible to write the rate of change of $\mathcal{O}$ as

$$\frac{\mathrm{d}\mathcal{O}}{\mathrm{d}t} = \int \frac{\mathrm{d}^3 k}{8\pi^3} \sum_{c,c'} \frac{\mathrm{d}\tilde{\rho}_{c\,c'}(\boldsymbol{k})}{\mathrm{d}t} \widetilde{\mathcal{O}}_{c'c}(\boldsymbol{k}) \,, \tag{3.57}$$

and considering the following definitions

$$\alpha \equiv \frac{e^2}{\mathrm{i}\hbar^2} \frac{1}{8\pi^3} \,, \tag{3.58}$$

$$\mathfrak{u}(\omega) \equiv \left(\frac{1}{\omega - \omega_{c'\nu} - \mathrm{i}\epsilon} - \frac{1}{\omega - \omega_{c\nu} + \mathrm{i}\epsilon} \right) \,, \tag{3.59}$$

then, we have that

$$\begin{aligned} \frac{\mathrm{d}\mathcal{O}}{\mathrm{d}t} = & \frac{e^2}{\mathrm{i}\hbar^2} \int \frac{\mathrm{d}^3 k}{8\pi^3} \sum_{\nu,c,c'} \widetilde{\mathcal{O}}_{c'c}\, r^a_{c\nu}\, r^b_{\nu c'} \left(\frac{1}{\omega - \omega_{c'\nu} - \mathrm{i}\epsilon} - \frac{1}{\omega - \omega_{c\nu} + \mathrm{i}\epsilon} \right) \\ & \times \; E^a(\omega)\, E^{b*}(\omega) \,, \\ = & \; \alpha \int \mathrm{d}^3 k \sum_{\nu,c,c'} \widetilde{\mathcal{O}}_{c'c}\, r^a_{c\nu}\, r^b_{\nu c'}\, \mathfrak{u}(\omega)\, E^a(\omega)\, E^{b*}(\omega) \,. \end{aligned} \tag{3.60}$$

Eq. 3.60 can be used to compute the spin–injection–rate $\dot{\mathbb{S}} \equiv \mathrm{d}\mathbb{S}/\,\mathrm{d}t$ if instead of using the arbitrary operator $\hat{o}$, we consider the spin operator $\hat{s}^i$, given by the Eqs. (3.10) and (3.11). Then

$$\dot{\hat{s}}^i = \; \alpha \int \mathrm{d}^3 k \sum_{\nu,c,c'} \hat{s}^i_{c'c}\, r^b_{c\nu}\, r^c_{\nu c'}\, \mathfrak{u}(\omega)\, E^b(\omega)\, E^{c*}(\omega) \,. \tag{3.61}$$

Using the time–reversal invariance

$$\omega_m(-\boldsymbol{k}) = \omega(\boldsymbol{k}) \,, \tag{3.62}$$

$$r^a_{mn}(-\boldsymbol{k}) = r^a_{nm}(\boldsymbol{k}) \,, \tag{3.63}$$

$$\hat{s}^i_{mn}(-\boldsymbol{k}) = \hat{s}^i_{nm}(\boldsymbol{k}) \,, \tag{3.64}$$

it is then possible to add the $\boldsymbol{k}$ and the $-\boldsymbol{k}$ contributions to the integral Eq. (3.61) and then

$$\dot{\hat{s}}^i = \alpha \int_{\boldsymbol{k}>0} \mathrm{d}^3k \sum_{\nu,c,c'} \left[\left(s^i_{c'c}\, r^b_{c\nu}\, r^c_{\nu c'} \right)\Big|_{\boldsymbol{k}} + \left(s^i_{c'c}\, r^b_{c\nu}\, r^c_{\nu c'} \right)\Big|_{-\boldsymbol{k}} \right] \mathfrak{u}(\omega) E^b\, E^{c*} \,. \tag{3.65}$$

Now, making the definition

$$\mathfrak{s}^{ibc} \equiv s^i_{c'c}\, r^b_{c\nu}\, r^c_{\nu c'} \,, \tag{3.66}$$

to simplify the notation and using the properties of Hermitian operators, $\mathrm{O}_{mn}(\boldsymbol{k}) = \mathrm{O}^*_{nm}(\boldsymbol{k})$, is then possible to write

$$\begin{aligned}
\dot{\hat{s}}^i = &\ \alpha \int_{\boldsymbol{k}>0} \mathrm{d}^3k \sum_{\nu,c,c'} \left[\mathfrak{s}^{ibc}\Big|_{\boldsymbol{k}} + \mathfrak{s}^{ibc}\Big|_{-\boldsymbol{k}} \right] \mathfrak{u}(\omega)\, E^b\, E^{c*} \,, \\
= &\ \alpha \frac{1}{2} \int_{\boldsymbol{k}>0} \mathrm{d}^3k \sum_{\nu,c,c'} \left[\mathfrak{s}^{ibc}\Big|_{\boldsymbol{k}} - \mathfrak{s}^{ibc\,*}\Big|_{\boldsymbol{k}} \right] \mathfrak{u}(\omega)\, E^b\, E^{c*} \,, \\
= &\ \alpha \int \mathrm{d}^3k \sum_{\nu,c,c'} \mathrm{Im}\left[\mathfrak{s}^{ibc} \right] \mathfrak{u}(\omega)\, E^b\, E^{c*} \,.
\end{aligned} \tag{3.67}$$

Using the relation

$$\lim_{\epsilon\to 0} \ \frac{1}{\omega - \omega_{c\nu} - i\epsilon} = P\left(\omega - \omega_{c\nu}\right) + \mathrm{i}\pi\delta\left(\omega - \omega_{c\nu}\right) \,, \tag{3.68}$$

where P means the "principal part". Then the Eq. (3.67) can be written as

$$\begin{aligned}
\dot{\hat{s}}^i = &\, \alpha \int \mathrm{d}^3k \sum_{\nu,c,c'} \mathrm{Im}\left[\mathfrak{s}^{ibc} \right] \left\{ P\left(\frac{1}{\omega - \omega_{c'\nu}} - \frac{1}{\omega - \omega_{c\nu}} \right) \right. \\
&\left. + i\pi \left[\delta(\omega - \omega_{c'\nu}) + \delta(\omega - \omega_{c\nu}) \right] \right\} E^b\, E^{c*} \,, \\
= &\, \alpha \int \mathrm{d}^3k \sum_{\nu,c,c'} \mathrm{Im}\left[\mathfrak{s}^{ibc} \right] \left\{ P\left(\frac{\omega_{c'c}}{(\omega - \omega_{c'\nu})(\omega - \omega_{c\nu})} \right) \right. \\
&\left. + i\pi \left[\delta(\omega - \omega_{c'\nu}) + \delta(\omega - \omega_{c\nu}) \right] \right\} E^b\, E^{c*} \,,
\end{aligned} \tag{3.69}$$

$$\dot{\hat{s}}^i \simeq \alpha \int \mathrm{d}^3k \sum_{\nu,c,c'}{}' \mathrm{Im}\left[\mathfrak{s}^{ibc} \right] \left[\delta(\omega - \omega_{c'\nu}) + \delta(\omega - \omega_{c\nu}) \right] E^b\, E^{c*} \,. \tag{3.70}$$

Since the term associated to the principal part is on the order of $\omega_{cc'}$ giving a weak contribution. The primed sum symbol indicates that the sum should be performed on pairs cc' of quasi–degenerate conduction bands. Instead of having tow resonance frequencies at $\omega = \omega_{c\nu}(\boldsymbol{k})$ and the other at $\omega = \omega_{c'\nu}(\boldsymbol{k})$ exist only one. To obtain this result it is necessary to change c by c' in the second δ to have

$$\dot{\hat{s}}^i = \zeta^{ibc} E^b(-\omega)\, E^{c*}(\omega)\,, \tag{3.71}$$

where

$$\widetilde{\zeta}^{ibc} = \alpha \int \mathrm{d}^3k \sum_{\nu,c,c'}{}' \,\mathrm{Im}\left[\mathfrak{s}^{ibc} + \mathfrak{s}'^{\,ibc}\right] \delta(\omega - \omega_{c\nu})\,, \tag{3.72}$$

from where $\mathfrak{s}^{ibc}$ is given by the Eq. (3.66) and $\mathfrak{s}'^{\,ibc}$ is took from Eq. (3.66) changing the values of c by c'. The $-\omega$ argument refers to the complex conjugate of the field in the frequency domain. This helps to clarify that the only resonant frequency is $\omega = \omega_{c\nu}(\boldsymbol{k})$. The Eq. (3.72) is known as the "spin–injection third–rank pseudo–tensor component" having the property that $\widetilde{\zeta}^{ibc} = -\widetilde{\zeta}^{ibc}$ [126] and being purely imaginary.

Both, the spin interaction rate, $\dot{\hat{s}}^i$, and the spin–injection pseudo–tensor component, $\widetilde{\zeta}^{ibc}$, describe the total spin injected to the conduction band. To completely describe the spin polarization it is necessary to consider it as an average of the electron spin, i.e., as the rate of the spin injection, $\dot{\hat{s}}^i$, with respect to the carrier injection rate, $\dot{n}$, to have the density spin polarization $\mathcal{D}^i$ in the given direction i

$$\mathcal{D}^{\,i} = \frac{\dot{\hat{s}}^i}{(\hbar/2)\dot{n}}\,, \tag{3.73}$$

where the "Fermi's golden rule[4]" derivation gives the carrier injection rate $\dot{n} \equiv \mathrm{d}n/\,\mathrm{d}t$

$$\dot{n} = \xi^{ib} E^i(-\omega)\, E^b(\omega)\,, \tag{3.74}$$

from where

$$\xi^{ib} \equiv 2\mathrm{i}\alpha \int \sum_{c,\nu} \mathrm{d}^3k\, r^i_{\nu c}(\boldsymbol{k})\, r^b_{c\nu}(\boldsymbol{k}) \delta\left[\omega_{c\nu}(\boldsymbol{k}) - \omega\right]\,. \tag{3.75}$$

[4]The Fermi's golden rule is a way to calculate the probability of transition per unit time from one energy eigenstate of a quantum system into a continuum of energy eigenstates, due to a perturbation [107]

$$W_{nk} = \frac{2\pi}{h}|V_{nk}|^2 \rho(E_k)$$

where $E_k = E_n$.

As was mentioned before regarding Eq. (3.71), the $-\omega$ argument refers again to the complex conjugate of the field.

Using a circularly polarized electric field along the xy–plane,

$$\boldsymbol{E}(\omega) = E_0(\hat{x} - \mathrm{i}\hat{y})/\sqrt{2}, \tag{3.76}$$

we obtain that Eq. (3.73) reduces to

$$\mathcal{D}^i = \frac{2}{\hbar}\frac{2\zeta^{ixy}}{\xi^{xx} + \xi^{yy}}, \tag{3.77}$$

and we obtain similar equations for polarization along xz and yz planes.

3.7 Summary

The main results of the chapter 3 corresponds from Eq. (3.77) to Eq. (3.75). The software, ABINIT and TINIBA, use the basis of this theoretical treatment in the calculations of this project. In the following chapter we will be describe the way both programs work together. Also there will be presented the results and conclusions of this thesis.

Chapter 4

Software, molecules, and results

Contents

To obtain the properties of graphane, we used the software TINIBA together with ABINIT. In the following section it will be explained some of the generalities about this software and how it has been used to obtain the results of this thesis and other scientific researches. Later we present the molecules to describe and the procedure to obtain their properties.

4.1 The software projects

As was mentioned before in section 3.5, the software ABINIT, developed in Belgium, took its name from the latin term *ab initio*, which means "from first principles", which is widely used in the literature of solid state physics, and when the method of plane waves, described in chapter 3, is used. On the other hand, the software TINIBA was developed at *Centro de Investigaciones en Óptica* (CIO) as a complement to ABINIT, adding functionality as a scientific research software.

4.1.1 ABINIT [127]

The ABINIT software project started in 1997. The initial goal was to create a software package for the *ab initio* study of material's properties. Thinking in users of Linux Operating Systems the developers of ABINIT decided to make a Free Software license to help the community of material scientists. The first publicly available version of ABINIT was released in December 2000. The developers community has grown to about fifty people.

Because of its large developer group, the capabilities of ABINIT can cover now a wide spectrum of properties like computation of equilibrium cell parameters and atomic positions, vibrational properties, prediction of phase (meta) stability or instability, elastic properties, dielectric and piezoelectric properties, non–linear optical properties, thermodynamic behaviour, electronic properties, magnetic properties, space group analysis, and more using parallelizating computation algorithms. Also this software is characterized because of its ease of use, its accompanying high–level documentation and brings to the user the capability to change the main software code.

ABINIT's main program is based in the "Density Functional Theory" described in section 3.3. For response functions, like vibrations, dielectric or piezoelectric properties, the specialized "Density Functional Perturbation Theory" has been implemented. However, selected electronic properties, in particular the prediction of electronic band gaps and the metallic or insulating character, can be computed accurately due to the implementation of the "Many–Body Perturbation Theory", the so–called "GW approximation."

ABINIT is based on the plane–wave expansion of the electronic wavefunctions, described in section 3.4, with a periodic representation of the system in a box under periodic boundary conditions. This representation is especially suitable to study any anisotropic media: the box is taken as the "primitive unit cell." Taking a non–primitive cell (called "super–cell") allows the study of systems in which the translational symmetry is reduced.

For metals, different smearing schemes allow to keep the number of such wavevectors reasonably small. Magnetism is also properly treated. Ferromagnetic as well as anti–ferromagnetic materials are as accessible as non–magnetic ones. Calculations including spin–orbit coupling and non–collinear magnetism are also possible.

Also, for a given geometry, ABINIT is able to compute analytically the forces on atoms and stresses on the cell. Such information is important in

order to start an optimization of atomic position an unit cell parameters like the generation of new trial geometries.

Is well known that in the treatment of the crystalline state symmetries plays an important role. There has been included in ABINIT a database of the 230 (Fedrov) space groups and the 1191 (Shubnikov) magnetic groups following the conventions used in the "International Tables for Crystallography". With this improvement different operations can be performed:

> Reconstruction of the atomic coordinates in the full primitive cell from its irreducible part.
> Identification of the space group if all atomic coordinates are given.
> Automatic determination of the symmetry operations.

Because electronic charge densities are the basic output of the 'Density Functional Theory, presented in section 3.3, it is possible to know the structure using this procedure. Also there was implemented the "GW methodology" to achieve more satisfactory description of the band structure an band gaps, with typical discrepancy less than 0.2 eV with respect to experimental data.

4.1.2 TINIBA

The software project called TINIBA[1] was developed at *Centro de Investigaciones en Óptica* (CIO).

TINIBA is a collection of routines to make calculations of optical responses in semiconductors using parallel computation in a cluster. Being a free software and written in languages of public domain like bash, pearl and fortran, TINIBA runs in the free operating system GNU/LINUX.

Using TINIBA is possible to make the automation of some calculations in parallel. Parallelization is needed because using a large number of computing cores, instead only one, the computation time is reduced to a fraction. Because in a culster is possible to have different infrastructures of computing cores, TINIBA, with the help of the user, is able to set up the workload destined to each core architecture and then optimize the computing time.

Some of the responses that TINIBA calculates are the Lineal Optical Response, Second Harmonic Generation and the Optical Spin Injection in elec-

[1] Special thanks to J. L. Cabellos for choosing the name of the software like ABINIT read backwards.

trons.

TINIBA can be executed, copied, distributed, changed and improved for every person[2] with the sufficient knowledge about the theme and programming languages previously mentioned. TINIBA and ABINIT use the mathematical and quantum background described in chapter 3.

In appendix A we show the International publications using TINIBA since it's creation of and to date when this thesis has been finished.

4.2 Graphane molecules

As was mentioned before, a graphane molecule is obtained when a graphene molecule is hydrogenated. Graphane can be obtained by different chemical procedures but our theme of interest is to characterize it using the quantum description presented in chapter 3 and the software presented in sections 4.1.1 and 4.1.2.

Graphene consists of a single layer of carbon molecules, as shown in Fig. (1.1). Some graphene layers can be stacked to produce bi–layered graphene and few–layered graphene. This is not the case when we talk about graphane because it is possible to have different bonds with hydrogen atoms and different proportions of hydrogenation to obtain different graphane molecules.

In this thesis was described and characterized only two of the possible graphane molecules corresponding to the so called $C_{16}H_{16}$–*chair* and $C_{16}H_8$–*up* molecules[3] shown in Fig. (4.1).

According to the theory of expansion in plane waves and the Bloch's theorem presented in chapter 3, we defined the unit cells for the lattices of both molecules to make the computational calculations in an more convenient way. The corresponding unit cells for the $C_{16}H_{16}$–*chair* and the $C_{16}H_8$–*up* molecules are shown in Fig. 4.2

[2] This is the main principle of the Free Software Foundation.

[3] With the same combination of atoms is possible to obtain the $C_{16}H_{16}$–*boat* and $C_{16}H_8$–*up–down* molecular structures, respectively.

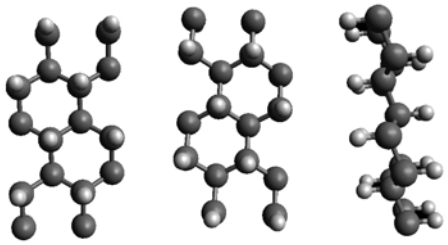

(a) $C_{16}H_{16}$–*chair*.

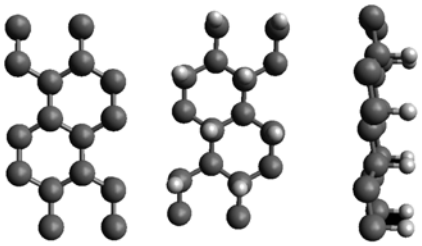

(b) $C_{16}H_8$–*up*.

Figure 4.1: Graphane molecules characterized in this thesis.

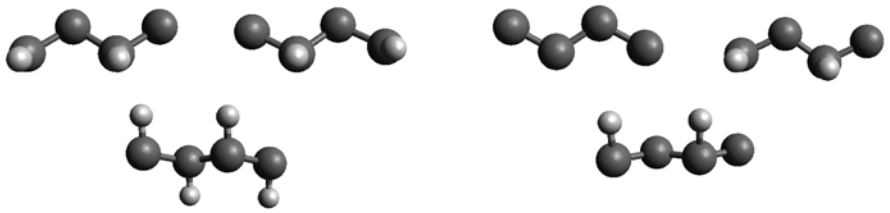

(a) $C_{16}H_{16}$–*chair* unit cell.

(b) $C_{16}H_8$–*up* unit cell.

Figure 4.2: Scheme of the unit cells corresponding to the molecules shown in Fig. (4.1).

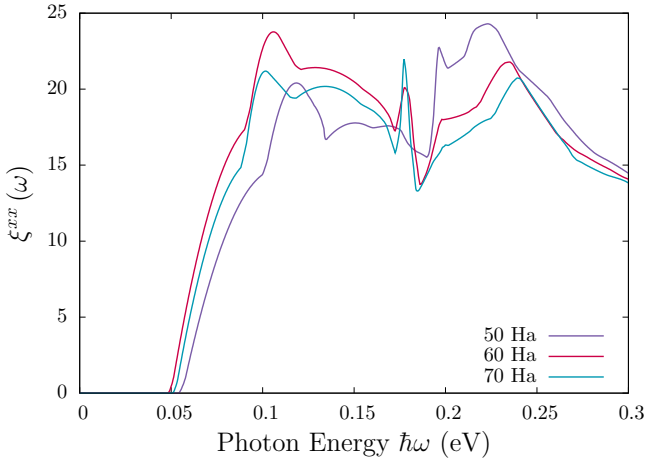

Figure 4.3: Convergence analysis for $\xi^{xx}(\omega)$ as a function of the energy cut–off. The number of K-points is 2314. The system is $C_{16}H_8$–*up*.

4.3 Procedure of calculations

We first obtain convergence of the results as a function of the energy cut-off, and then the corresponding convergence as a function of K–points [128]. So, using different values for the Energy Cutoff chosen by "trial–and–error" we reach the convergence. Once the convergence of the Energy Cutoff is reached we chose different values for the K–points, till the carrier injection tensor $\xi^{ij}(\omega)$ and the spin polarization tensor $\zeta^{ijk}(\omega)$ are converged.

4.4 Results

The results were obtained following the procedure explained in section 4.3 and using the unit cells shown in Fig. (4.2). The next two subsections are for the two different graphane structures discussed before.

4.4.1 $C_{16}H_8$–*up* molecule

In Figs. (4.3) and (4.4) we show the convergence of $\xi^{xx}(\omega)$ and $\zeta^{xxy}(\omega)$ as a function of the energy cut–off. We see that a very high energy is required for convergence, and that, even for 70 Ha, the results still show some deviation

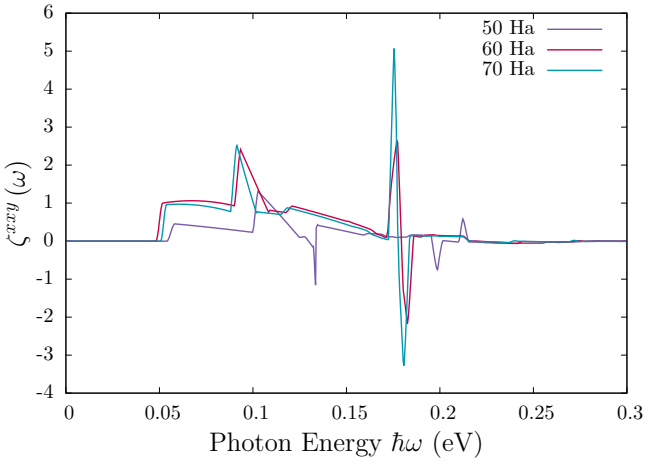

Figure 4.4: Convergence analysis for $\zeta^{xxy}(\omega)$ as a function of the energy cut–off. The number of K-points is 2314. The system is $C_{16}H_8$–*up*.

from the 60 Ha values. However, $\mathcal{D}^i(\omega)$, shows an adequate convergence for cut–off energies between 60 and 70 Ha, as shown in Fig. 4.5. The number of K–points used, 2314, is already the minimum value for convergence.

In Fig. 4.6 we show (converged) $\mathcal{D}^i(\omega)$ for the incoming field polarized (circularly) along xy, xz and yz planes, then, the field propagates along z, y and x, respectively. We see that the largest value for the degree of spin polarization comes from light propagating perpendicular to the plane of the system, and gives a 100% spin polarization along x, whereas along z is an still sizable 80%. Along y is only 25%. For the other two polarizations along xz and yz we obtain values below $\sim 20\%$, for $\mathcal{D}^i(\omega)$ with $i = x, y, z$.

We also notice that the maximum of $\mathcal{D}^i(\omega)$ occurs right at the energy gap of the system. This indicates that the optical transition induced by the incoming field polarize the system at the onset with maximum probability. The percentage of $\mathcal{D}^i$ means that we can re-orient the spin of the electrons along the direction of the incoming field, by that amount. However, when is negative, as shown, for the xz–polarization, it means that the spin polarize opposite to the direction of the field, in this case, along $-x$, $-y$ and $-z$. We finally mention that the energy region corresponds to infrared frequencies.

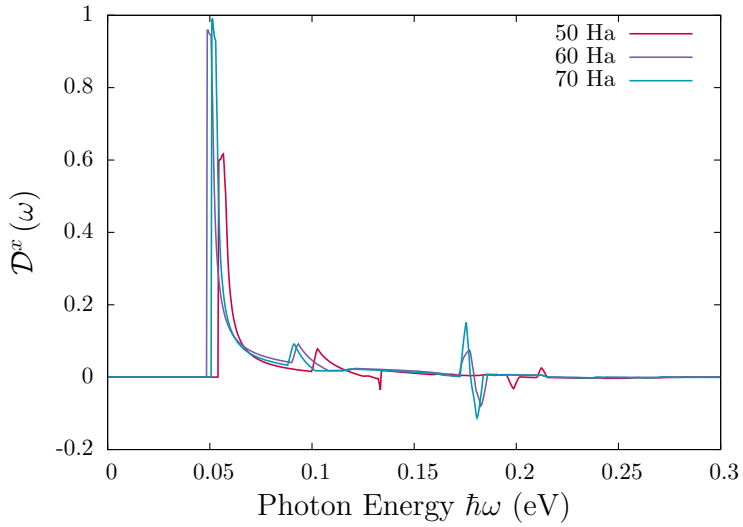

Figure 4.5: Convergence analysis for $\mathcal{D}^x(\omega)$ as a function of the energy cut–off. The number of K-points is 2314. The system is $C_{16}H_8$–*up*.

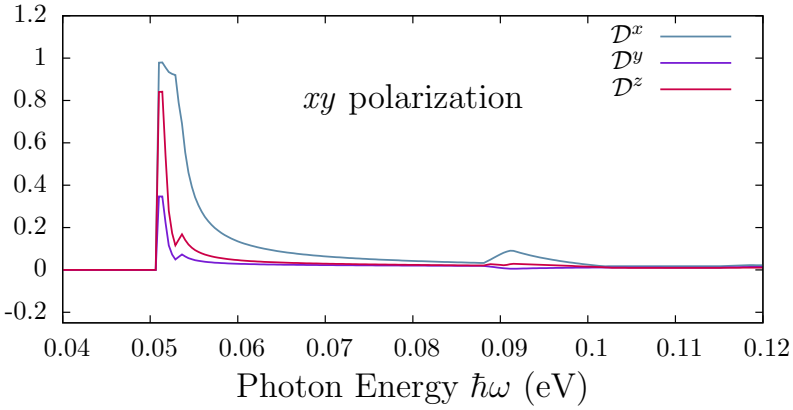

Figure 4.6: $\mathcal{D}^i(\omega)$ for xy polarization of the incoming circularly incident electric field. The system is $C_{16}H_8$–*up*.

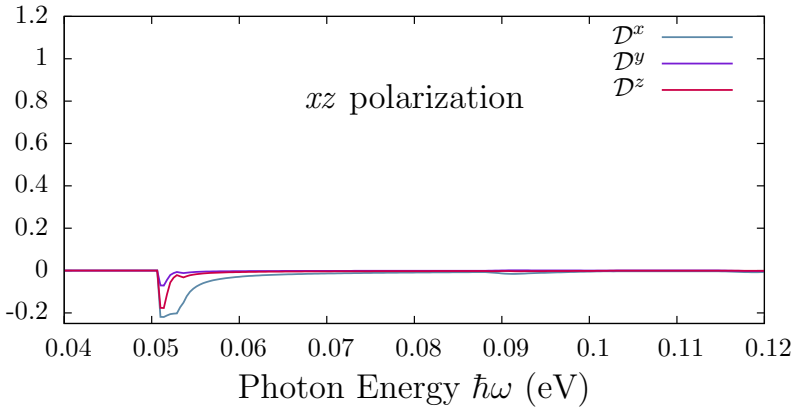

Figure 4.7: $\mathcal{D}^i(\omega)$ for xz polarization of the incoming circularly incident electric field. The system is $C_{16}H_8$–*up*.

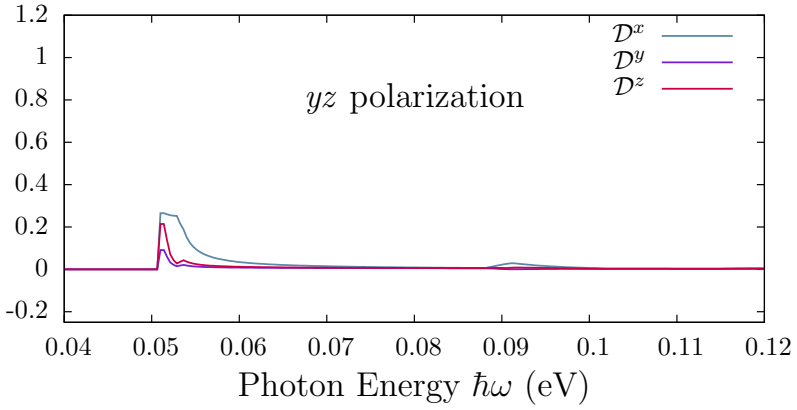

Figure 4.8: $\mathcal{D}^i(\omega)$ for yz polarization of the incoming circularly incident electric field. The system is $C_{16}H_8$–*up*.

4.4.2 $C_{16}H_{16}$–*chair* molecule

In Fig. 4.9 we show (converged) $\mathcal{D}^y(\omega)$ and $\mathcal{D}^z(\omega)$ for the incoming field polarized (circularly) along xy. We see that the largest value for the degree of spin polarization is along y and is only 0.1%! and it also occurs right at the energy gap of the system, as in the previous case. This very low value for the degree of spin polarization, rules out this graphane hydrogenated sample as a viable system to polarize spin. Thus, we just explain where this small value is coming from. Indeed, in Fig. 4.10 we show $\xi^{xx,yy}$ and ζ^{zxy} for energies around the gap. We see that both ξ^{xx} and ξ^{yy} rise very sharply, indicating that at the onset of the electronic transitions the number of injected carriers is very large. Then, although, ζ^{zxy} also raises sharply, when we divide it over $\xi^{xx}+\xi^{yy}$, as required by Eq. (3.77), we quench $\mathcal{D}^i(\omega)$ very dramatically, thus giving very small values. To corroborate this point, in Fig. 4.11, we show the $\xi^{xx,yy}$ and ζ^{xxy} for graphane $C_{16}H_8$–*up*, where we notice that whereas $\xi^{xx,yy}$ rises sharply at the energy gap, both ξ^{xx} and ξ^{yy} start off more softly, thus when we calculate $\mathcal{D}^i(\omega)$ we obtain the very large value seen in Fig. 4.6. Therefore we may say that in order to get large values of the degree of spin polarization, we need systems for which the rate of carrier injection starts off slowly at the energy gap.

To stress this point even further, in Fig. (4.12) we show the electronic band structures for the $C_{16}H_8$–*up* (Fig. 4.12b) and $C_{16}H_{16}$–*chair* (Fig. 4.12a). The lines in red are the valence bands and the ones in blue the conduction bands. The vertical arrows corresponds to allowed electronic transitions between the top valence and bottom conduction band for the corresponding energy gap plus a tolerance of 10%. We see that for the $C_{16}H_{16}$–*chair* system there are more transitions from the valence to the conduction band than in for the $C_{16}H_8$–*up* system, specially those coming around the K-point. Since the number of injected carriers, as characterized by $\xi^{ii}(\omega)$, is proportional to the number of transitions, we see that indeed, the $C_{16}H_{16}$–*chair* system will have more injected carriers around the energy gap, than the $C_{16}H_8$–*up* system. Thus, we obtain a very tiny fraction of spins polarized for $C_{16}H_{16}$–*chair* .

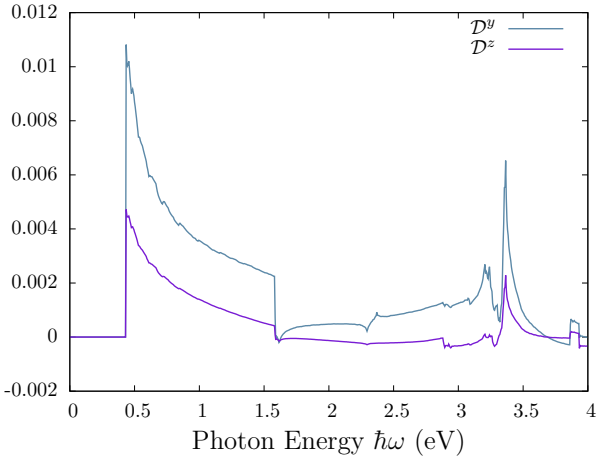

Figure 4.9: $\mathcal{D}^i(\omega)$ for xy polarization of the incoming circularly incident electric field. $C_{16}H_{16}$–*chair* molecule.

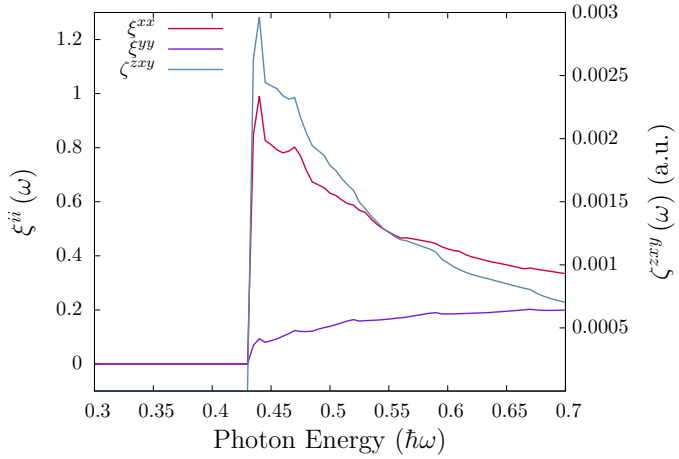

Figure 4.10: Comparison between the ξ^{ii} and ζ^{zxy} for $C_{16}H_{16}$–*chair*.

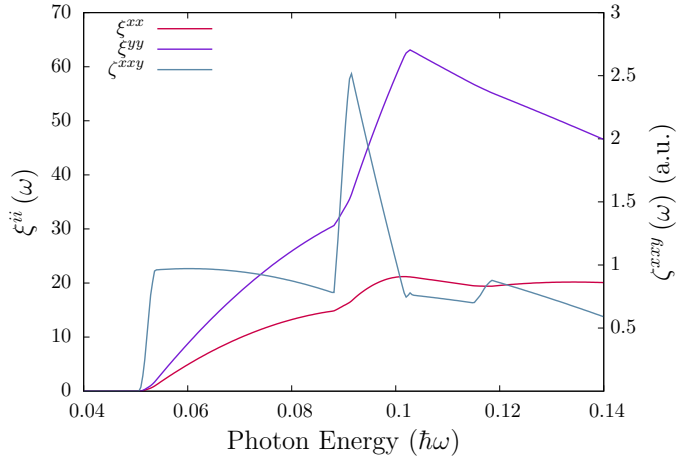

Figure 4.11: Comparison between the ξ^{ii} and ζ^{xxy} for $C_{16}H_8$–*up*.

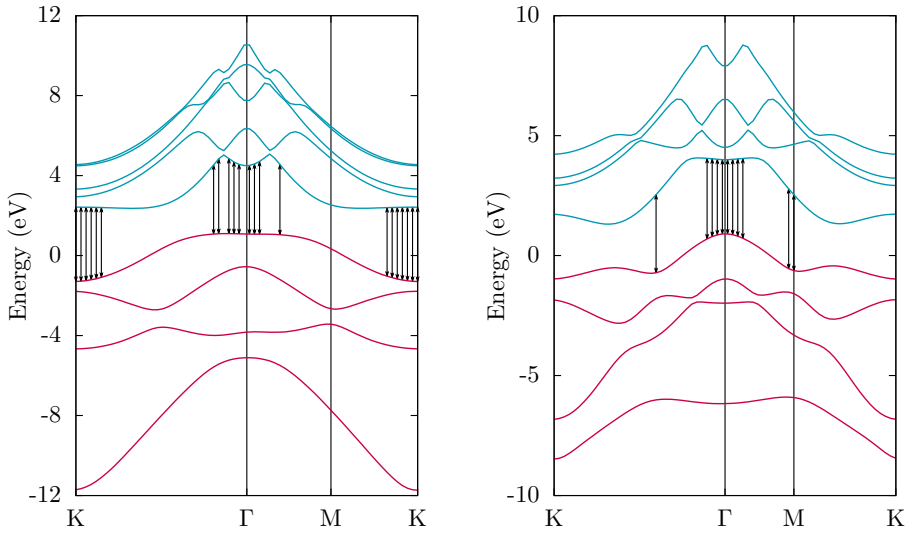

(a) $C_{16}H_{16}$–*chair*. (b) $C_{16}H_8$–*up*.

Figure 4.12: Comparison of band structures for the systems. The vertical arrows indicate the allowed transitions between the top valence (red) and bottom conduction (blue) bands for the corresponding energy gap plus a 10% of tolerance.

4.5 Chapter conclusions

For our systems we have that the $C_{16}H_8$–*up* is more spin–polarizable than the $C_{16}H_{16}$–*chair*. The $\mathcal{D}^i(\omega)$ depends on the interplay between the possibility for polarizing the spin of the electrons and the number of carriers that is possible to inject.

Chapter 5

Conclusions and perspectives

Contents

5.1 Conclusions

The analysis presented in this thesis could determine the possibility of inducing optical spin polarization in a material. We found for our systems that the $C_{16}H_8$–*up* is more spin–polarizable than the $C_{16}H_{16}$–*chair*. For the $C_{16}H_8$–*up* system, the largest value of the degree of spin polarization comes from light propagating perpendicular to the plane of the system giving a 100% spin polarization along x, whereas along z is also rather large at 80%. On the other hand, the largest value for the degree of spin polarization in the $C_{16}H_{16}$–*chair* system was obtained for the $\mathcal{D}^y$ using xy polarization. The corresponding low value was near to 1%.

We have that the structural basis of both compounds is carbon and both have a planar hexagonal honeycomb lattice. According to that we can conclude that the level of hydrogenation and the bond structures determines the behavior of $\xi^{ii}(\omega)$ and $\zeta^{ijk}(\omega)$ and so the possibility to have a larger or lesser spin injection.

The $\mathcal{D}^i(\omega)$ directly depends on the interplay between the possibility to polarizing the spin of the electrons and the number of carriers that is possible to inject. So, when the incident beam reaches the sample gap and starts the absorption of energy, thus promoting the carriers to the conduction bands,

it is better for our propose if this "turning–on" of the absorption is slower than that responsible for polarizing the spin.

The optical spin injection has been studied in different materials. In Ref. [129] an study of the stress–modulated optical spin injection in GaAs and Si semiconductors is presented. According to the article, the maximum optical spin polarization obtained for Si was 50%. On the other hand, in Ref. [130] the optical spin polarization of CdSe was characterized, and they found a 100% of polarization at the band edge. According to that the our $C_{16}H_8$–*up–down* system is suitable to be used in optical spin injection applications. This is a really promissory result for a large number of Spintronics applications.

5.2 Perspectives

For the future work we are interested in the study and characterizing of more graphane structures, like $C_{16}H_{16}$–*boat* and $C_{16}H_8$–*up–down*, in order to describe the possibility to induce optical spin polarization and describe the band structure for all graphanes. From the theoretical point of view we would like to include "Many–Body" effects at the GW approximation in order to achieve more accurate results, in particular, the determination of the energy gap.

Appendix A

Publications made at *Centro de Investigaciones en Óptica* using TINIBA:

Electronic entanglement via quantum Hall interferometry in analogy to an optical method, Frustaglia, Diego and Cabellos, Adrian, Phys. Rev. B 80, 201312(R) (2009).

Stress–modulated optical spin injection in bulk Si *and* GaAs *semiconductors*, Cabellos, J. L., Salazar, Cuauhtémoc and Mendoza, Bernardo S, Phys. Rev. B 80, 245204 (2009).

Spin–Orbit Effects on the Optical Anisotropy of Semiconductor Surfaces, R. A. Vázquez–Nava, B. S. Mendoza and N. Arzate, Phys. Stat. sol. (b) 242, 3022 (2005).

Layer–by–layer analysis of the linear optical response of clean and hydrogenated Si(100) *surface*, B. Mendoza, N. Arzate, F. Nastos and J. Sipe, Phys. Rev. B 74, 075318 (2006).

Second–harmonic and reflectance–anisotropy spectroscopy of vicinal Si(001) */SiO*22 *interfaces: Experiment and simplified microscopic model*, Jinhee Kwon, M. C. Downer and B. S. Mendoza, Phys. Rev. B 73, 195330 (2006).

Second harmonic surface response of a composite, Bernardo S. Mendoza and W. Luis Mochán, Optical Materials 29, 1–5 (2006).

Full band structure LDA and $\mathbf{k} \cdot \mathbf{p}$ *calculations of optical spin–injection*, F. Nastos, J. Rioux, M. Strimas–Mackey, Bernardo S. Mendoza, and J. E. Sipe Phys. Rev. B, 76, 205113 (2007).

Theoretical study of the optical response of the adsorption of Sb *on the* GaAs(110) *surface*, Bernardo S. Mendoza, N. Arzate and R.A. Vázquez–Nava, Phys. Stat. Sol. (c) 8, 2604–2609 (2008).

Effective optical response of metamaterials, Guillermo P. Ortiz, Brenda E. Martínez–Zérega, Bernardo S. Mendoza, and W. Luis Mochán, Phys. Rev. B 79, 245132–1–9 (2009).

Effects of nonlocality on second–harmonic generation in bulk sem-iconductors, J.L. Cabellos, Bernardo S. Mendoza, M.A. Escobar, F. Nastos and J. Sipe,

Phys. Rev. B 80, 155205–1–13 (2009). Citas página: 68.

Stress modulated optical spin–injection in bulk Si *and* GaAs *semiconductors*, J.L. Cabellos, C. Salazar and Bernardo S. Mendoza, Phys. Rev. B. 80 245204–1–5 (2009).

Optical spin injection in semiconductors, Bernardo S. Mendoza, J.L. Cabellos, and C. Salazar Modern Physics Letters B 24, 1507–1522 (2010).

Reflectance anisotropy spectra of CdTe(001) *surfaces*, Raúl Vázquez–Nava, N. Arzate and Bernardo S. Mendoza, Phys. Status Solidi B 247, 1979–1983 (2010).

Second harmonic response of the Si(111)7 $\times$ 7 *surface*, J.E. Mejía, Bernardo S. Mendoza and Kjeld Pedersen, Surface Science 605, 941–946 (2011).

Optical absorption spectroscopy of one–dimensional silicon nanostructures, N. Arzate, R.A. Vaáquez–Nava, J.L. Cabellos, R. Carriles, E. Castro–Camus, M.E. Figueroa–Delgadillo and B.S. Mendoza, Optics and Lasers in Engineering, 49 668–674 (2011).

Coherent effects in the sum–frequency generation at randomly rough surfaces, M. Leyva–Lucero, Bernardo S. Mendoza, E. Méndez and C. Valencia, J. Opt. Soc. Am B, 28 1882–1894 (2011).

Second–harmonic spectroscopic study of silicon nanocrystals embedded in SiO2, Junwei Wei, Adrian Wirth, Michael Downer and Bernardo S. Mendoza, Physical Review B, 84 165316 (2011).

Optical coherent current control at surfaces: Theory of injection current, J. L. Cabellos, Bernardo S. Mendoza, and A. I. Shkrebtii, Physical Review B, 84 195326 (2011).

Optical spin injection at semiconductor surfaces, Bernardo S. Mendoza and J.L. Cabellos Phys. Rev. B 85, 165324 (2012).

Graphene and graphane functionalization with hydrogen: electronic and optical signatures, A. I. Shkrebtii, E. Heritage, P. McNelles, J. L. Cabellos and B. S. Mendoza, Phys. Status Solidi C 9, 1378–1383 (2012).

References

[1] A.K. Geim and K.S. Novoselov. The rise of graphene. *Nature Materials*, 6(3):183–191, 2007.

[2] C.N.R. Rao, K. Biswas, K.S. Subrahmanyam, and A. Govindaraj. Graphene, the new nanocarbon. *J. Mater. Chem.*, 19(17):2457–2469, 2009.

[3] H.P. Boehm, R. Setton, and E. Stumpp. Nomenclature and terminology of graphite intercalation compounds. *Carbon*, 24(2):241–245, 1986.

[4] H.P. Boehm, A. Clauss, G.O. Fischer, and U. Hofmann. Das adsorptionsverhalten sehr dünner kohlenstoff-folien. *Zeitschrift für anorganische und allgemeine Chemie*, 316(3-4):119–127, 1962.

[5] K.S. Novoselov, A.K. Geim, S.V. Morozov, D. Jiang, M.I.K.I.V. Grigorieva, S.V. Dubonos, and A.A. Firsov. Two-dimensional gas of massless dirac fermions in graphene. *Nature*, 438(7065):197–200, 2005.

[6] Y. Zhang, Y.W. Tan, H.L. Stormer, and P. Kim. Experimental observation of the quantum hall effect and berry's phase in graphene. *Nature*, 438(7065):201–204, 2005.

[7] K.S. Novoselov, Z. Jiang, Y. Zhang, S.V. Morozov, H.L. Stormer, U. Zeitler, J.C. Maan, G.S. Boebinger, P. Kim, and A.K. Geim. Room-temperature quantum hall effect in graphene. *Science*, 315(5817):1379–1379, 2007.

[8] K.S. Novoselov, A.K. Geim, S.V. Morozov, D. Jiang, Y. Zhang, S.V. Dubonos, I.V. Grigorieva, and A.A. Firsov. Electric field effect in atomically thin carbon films. *Science*, 306(5696):666–669, 2004.

[9] M.Y. Han, B. Özyilmaz, Y. Zhang, and P. Kim. Energy band-gap engineering of graphene nanoribbons. *Physical Review Letters*, 98(20):206805, 2007.

[10] C. Lee, X. Wei, J.W. Kysar, and J. Hone. Measurement of the elastic properties and intrinsic strength of monolayer graphene. *Science*, 321(5887):385–388, 2008.

[11] R.R. Nair, P. Blake, A.N. Grigorenko, K.S. Novoselov, T.J. Booth, T. Stauber, N.M.R. Peres, and A.K. Geim. Fine structure constant defines visual transparency of graphene. *Science*, 320(5881):1308–1308, 2008.

[12] D. Li and R.B. Kaner. Graphene-based materials. *Nat. Nanotechnol*, 3:101, 2008.

[13] M.I. Katsnelson. Graphene: carbon in two dimensions. *Materials today*, 10(1):20–27, 2007.

[14] C.N.R. Rao, A.K. Sood, R. Voggu, and K.S. Subrahmanyam. Some novel attributes of graphene. *The Journal of Physical Chemistry Letters*, 1(2):572–580, 2010.

[15] Sergey Mikhailov, editor. *Physics and Applications of Graphene - Theory*. InTech, 2011.

[16] E.V. Castro, K.S. Novoselov, S.V. Morozov, N.M.R. Peres, J.M.B.L. Dos Santos, J. Nilsson, F. Guinea, A.K. Geim, and A.H.C. Neto. Biased bilayer graphene: semiconductor with a gap tunable by the electric field effect. *Physical review letters*, 99(21):216802, 2007.

[17] Y. Zhang, T.T. Tang, C. Girit, Z. Hao, M.C. Martin, A. Zettl, M.F. Crommie, Y.R. Shen, and F. Wang. Direct observation of a widely tunable bandgap in bilayer graphene. *Nature*, 459(7248):820–823, 2009.

[18] H. Hibino, H. Kageshima, and M. Nagase. Epitaxial few-layer graphene: towards single crystal growth. *Journal of Physics D: Applied Physics*, 43:374005, 2010.

[19] C.N.R. Rao, A.K. Sood, K.S. Subrahmanyam, and A. Govindaraj. Graphene: The new two-dimensional nanomaterial. *Angewandte Chemie International Edition*, 48(42):7752–7777, 2009.

[20] S. Park and R.S. Ruoff. Chemical methods for the production of graphenes. *Nature nanotechnology*, 4(4):217–224, 2009.

[21] E. Stolyarova, K.T. Rim, S. Ryu, J. Maultzsch, P. Kim, L.E. Brus, T.F. Heinz, M.S. Hybertsen, and G.W. Flynn. High-resolution scanning tunneling microscopy imaging of mesoscopic graphene sheets on an insulating surface. *Proceedings of the National Academy of Sciences*, 104(22):9209, 2007.

[22] A. Gupta, G. Chen, P. Joshi, S. Tadigadapa, and P.C. Eklund. Raman scattering from high-frequency phonons in supported n-graphene layer films. *Nano letters*, 6(12):2667–2673, 2006.

[23] A.C. Ferrari. Raman spectroscopy of graphene and graphite: Disorder, electron–phonon coupling, doping and nonadiabatic effects. *Solid State Communications*, 143(1):47–57, 2007.

[24] A.C. Ferrari, J.C. Meyer, V. Scardaci, C. Casiraghi, M. Lazzeri, F. Mauri, S. Piscanec, D. Jiang, K.S. Novoselov, S. Roth, et al. Raman spectrum of graphene and graphene layers. *Physical Review Letters*, 97(18):187401, 2006.

[25] M.A. Pimenta, G. Dresselhaus, M.S. Dresselhaus, L.G. Cancado, A. Jorio, and R. Saito. Studying disorder in graphite-based systems by raman spectroscopy. *Phys. Chem. Chem. Phys.*, 9(11):1276–1290, 2007.

[26] D. Graf, F. Molitor, K. Ensslin, C. Stampfer, A. Jungen, C. Hierold, and L. Wirtz. Spatially resolved raman spectroscopy of single-and few-layer graphene. *Nano letters*, 7(2):238–242, 2007.

[27] J. Wu, W. Pisula, and K. Mullen. Graphenes as potential material for electronics. *Chemical reviews*, 107(3):718, 2007.

[28] R.Q. Zhang, T.S. Chu, C.S. Lee, and S.T. Lee. A theoretical study on the interactions of hydrogen species with various carbon and boron nitride phases. *The Journal of Physical Chemistry B*, 104(29):6761–6766, 2000.

[29] L. Bergman, M.T. McClure, J.T. Glass, and R.J. Nemanich. The origin of the broadband luminescence and the effect of nitrogen doping on the optical properties of diamond films. *Journal of applied physics*, 76(5):3020–3027, 1994.

[30] P. Kania and P. Oelhafen. Photoluminescence study of< 100> textured cvd diamonds. *Diamond and related materials*, 4(4):425–428, 1995.

[31] A.G.A. Rusli and S.R. Silva. Photoluminescence in amorphous carbon thin films and its relation to the microscopic properties. *Thin Solid Films*, 270(1-2):160–164, 1995.

[32] J.E. Bourée, C. Godet, B. Drévillon, R. Etemadi, T. Heitz, J. Cernogora, and J.L. Fave. Optical and luminescence properties

of polymer-like ac: H films deposited in a dual-mode pecvd reactor. *Journal of non-crystalline solids*, 198:623–627, 1996.

[33] S. Liu, S. Gangopadhyay, G. Sreenivas, S.S. Ang, and H.A. Naseem. Photoluminescence studies of hydrogenated amorphous carbon and its alloys. *Journal of applied physics*, 82:4508, 1997.

[34] Q. Zhang, S.C. Bayliss, and W. Frentrup. The stable blue and unstable uv photoluminescence from carbon nanoclusters embedded in SiO_2 matrices. *Solid state communications*, 99(12):883–886, 1996.

[35] V. Capozzi, G. Casamassima, G.F. Lorusso, A. Minafra, R. Piccolo, T. Trovato, and A. Valentini. Optical spectra and photoluminescence of C_{60} thin films. *Solid State Communications*, 98(9):853–858, 1996.

[36] J. Wagner and P. Lautenschlager. Hard amorphous carbon studied by ellipsometry and photoluminescence. *Journal of applied physics*, 59(6):2044–2047, 1986.

[37] R.C. Fang. Emission properties of amorphous silicon and carbon films. *Journal of luminescence*, 48:631–635, 1991.

[38] S. Xu, M. Hundhausen, J. Ristein, B. Yan, and L. Ley. Influence of substrate bias on the properties of ac: H films prepared by plasma cvd. *Journal of non-crystalline solids*, 164:1127–1130, 1993.

[39] W.A. Nevin, H. Yamagishi, M. Yamaguchi, and Y. Tawada. Emission of blue light from hydrogenated amorphous silicon carbide. *Nature*, 1994.

[40] R.Q. Zhang, E. Bertran, and S.T. Lee. Size dependence of energy gaps in small carbon clusters: the origin of broadband luminescence. *Diamond and related materials*, 7(11):1663–1668, 1998.

[41] Jian Ru Gong. *Graphene–Synthesis, Characterization, Properties and, Applications*. In Tech, 2011.

[42] S. Park, J. An, I. Jung, R.D. Piner, S.J. An, X. Li, A. Velamakanni, and R.S. Ruoff. Colloidal suspensions of highly reduced graphene oxide in a wide variety of organic solvents. *Nano letters*, 9(4):1593–1597, 2009.

[43] W.S. Hummers Jr and R.E. Offeman. Preparation of graphitic oxide. *Journal of the American Chemical Society*, 80(6):1339–1339, 1958.

[44] S.K. Pati, T. Enoki, and C.N.R. Rao. *Graphene and its fascinating attributes*. World Scientific Publishing Company, 2011.

[45] M. Choucair, P. Thordarson, and J.A. Stride. Gram-scale production of graphene based on solvothermal synthesis and sonication. *Nature Nanotechnology*, 4(1):30–33, 2008.

[46] Y. Hernandez, V. Nicolosi, M. Lotya, F.M. Blighe, Z. Sun, S. De, I.T. McGovern, B. Holland, M. Byrne, Y.K. Gun'Ko, et al. High-yield production of graphene by liquid-phase exfoliation of graphite. *Nature Nanotechnology*, 3(9):563–568, 2008.

[47] M. Lotya, Y. Hernandez, P.J. King, R.J. Smith, V. Nicolosi, L.S. Karlsson, F.M. Blighe, S. De, Z. Wang, I.T. McGovern, et al. Liquid phase production of graphene by exfoliation of graphite in surfactant/water solutions. *Journal of the American Chemical Society*, 131(10):3611–3620, 2009.

[48] C. Berger, Z. Song, T. Li, X. Li, A.Y. Ogbazghi, R. Feng, Z. Dai, A.N. Marchenkov, E.H. Conrad, N. Phillip, et al. Ultrathin epitaxial graphite: 2d electron gas properties and a route toward graphene-based nanoelectronics. *The Journal of Physical Chemistry B*, 108(52):19912–19916, 2004.

[49] E. Rollings, G.H. Gweon, S.Y. Zhou, B.S. Mun, J.L. McChesney, B.S. Hussain, A.V. Fedorov, P.N. First, W.A. De Heer, and A. Lanzara. Synthesis and characterization of atomically thin graphite films on a silicon carbide substrate. *Journal of Physics and Chemistry of Solids*, 67(9-10):2172–2177, 2006.

[50] K.V. Emtsev, A. Bostwick, K. Horn, J. Jobst, G.L. Kellogg, L. Ley, J.L. McChesney, T. Ohta, S.A. Reshanov, J. Röhrl, et al. Towards wafer-size graphene layers by atmospheric pressure graphitization of silicon carbide. *Nature materials*, 8(3):203–207, 2009.

[51] A. Reina, X. Jia, J. Ho, D. Nezich, H. Son, V. Bulovic, M.S. Dresselhaus, and J. Kong. Large area, few-layer graphene films on arbitrary substrates by chemical vapor deposition. *Nano letters*, 9(1):30–35, 2008.

[52] C.N.R. Rao, K.S. Subrahmanyam, H.S.S. Ramakrishna Matte, U. Maitra, K. Moses, and A. Govindaraj. Graphene: synthesis, functionalization and properties. *International Journal of Modern Physics B*, 25(30):4107, 2011.

[53] H.C. Schniepp, J.L. Li, M.J. McAllister, H. Sai, M. Herrera-Alonso, D.H. Adamson, R.K. Prud'homme, R. Car, D.A. Saville, and I.A. Aksay. Functionalized single graphene sheets derived from splitting graphite oxide. *The Journal of Physical Chemistry B*, 110(17):8535–8539, 2006.

[54] K.S. Subrahmanyam, S.R.C. Vivekchand, A. Govindaraj, and C.N.R. Rao. A study of graphenes prepared by different methods: characterization, properties and solubilization. *J. Mater. Chem.*, 18(13):1517–1523, 2008.

[55] S. Stankovich, D.A. Dikin, R.D. Piner, K.A. Kohlhaas, A. Kleinhammes, Y. Jia, Y. Wu, S.B.T. Nguyen, and R.S. Ruoff. Synthesis of graphene–based nanosheets via chemical reduction of exfoliated graphite oxide. *Carbon*, 45(7):1558–1565, 2007.

[56] O.E. Andersson, B.L.V. Prasad, H. Sato, T. Enoki, Y. Hishiyama, Y. Kaburagi, M. Yoshikawa, and S. Bandow. Structure and electronic properties of graphite nanoparticles. *Physical Review B*, 58(24):16387, 1998.

[57] B.L.V. Prasad, H. Sato, T. Enoki, Y. Hishiyama, Y. Kaburagi, A.M. Rao, P.C. Eklund, K. Oshida, and M. Endo. Heat–treatment effect on the nanosized graphite π–electron system during diamond to graphite conversion. *Physical Review B*, 62(16):11209, 2000.

[58] X. Li, W. Cai, J. An, S. Kim, J. Nah, D. Yang, R. Piner, A. Velamakanni, I. Jung, E. Tutuc, et al. Large–area synthesis of high–quality and uniform graphene films on copper foils. *Science*, 324(5932):1312–1314, 2009.

[59] E. Loginova, N.C. Bartelt, P.J. Feibelman, and K.F. McCarty. Evidence for graphene growth by c cluster attachment. *New Journal of Physics*, 10:093026, 2008.

[60] E. Starodub, S. Maier, I. Stass, N.C. Bartelt, P.J. Feibelman, M. Salmeron, and K.F. McCarty. Graphene growth by metal etching on ru (0001). *Physical Review B*, 80(23):235422, 2009.

[61] K.S. Subrahmanyam, L.S. Panchakarla, A. Govindaraj, and C.N.R. Rao. Simple method of preparing graphene flakes by an arc–discharge method. *The Journal of Physical Chemistry C*, 113(11):4257–4259, 2009.

[62] L.S. Panchakarla, K.S. Subrahmanyam, S.K. Saha, A. Govindaraj, H.R. Krishnamurthy, U.V. Waghmare, and C.N.R. Rao. Synthesis, structure, and properties of boron-and nitrogen-doped graphene. *Advanced Materials*, 21(46):4726–4730, 2009.

[63] C.N.R. Rao and A. Govindaraj. Nanotubes and nanowires, rsc nanoscience & nanotechnology series, 2005.

[64] A. Müller and A.K. Cheetham. *Nanomaterials chemistry: recent developments and new directions*. Vch Verlagsgesellschaft Mbh, 2007.

[65] S. Niyogi, E. Bekyarova, M.E. Itkis, J.L. McWilliams, M.A. Hamon, and R.C. Haddon. Solution properties of graphite and graphene. *Journal of the American Chemical Society*, 128(24):7720–7721, 2006.

[66] E. Bekyarova, M.E. Itkis, P. Ramesh, C. Berger, M. Sprinkle, W.A. De Heer, and R.C. Haddon. Chemical modification of epitaxial graphene: spontaneous grafting of aryl groups. *Journal of the American Chemical Society*, 131(4):1336–1337, 2009.

[67] K.A. Worsley, P. Ramesh, S.K. Mandal, S. Niyogi, M.E. Itkis, and R.C. Haddon. Soluble graphene derived from graphite fluoride. *Chemical Physics Letters*, 445(1-3):51–56, 2007.

[68] K.S. Subrahmanyam, A. Ghosh, A. Gomathi, A. Govindaraj, and C.N.R. Rao. Covalent and noncovalent functionalization and solubilization of graphene. *Nanoscience and Nanotechnology Letters*, 1(1):28–31, 2009.

[69] T. Ohta, A. Bostwick, T. Seyller, K. Horn, and E. Rotenberg. Controlling the electronic structure of bilayer graphene. *Science*, 313(5789):951–954, 2006.

[70] A. Das, S. Pisana, B. Chakraborty, S. Piscanec, S.K. Saha, U.V. Waghmare, K.S. Novoselov, H.R. Krishnamurthy, A.K. Geim, A.C. Ferrari, et al. Monitoring dopants by raman scattering in an electrochemically top-gated graphene transistor. *Nature Nanotechnology*, 3(4):210–215, 2008.

[71] R. Voggu, B. Das, C.S. Rout, and C.N.R. Rao. Effects of charge transfer interaction of graphene with electron donor and acceptor molecules examined using raman spectroscopy and cognate techniques. *Journal of Physics: Condensed Matter*, 20:472204, 2008.

[72] K.S. Subrahmanyam, R. Voggu, A. Govindaraj, and C.N.R. Rao. A comparative raman study of the interaction of electron donor and acceptor molecules with graphene prepared by different methods. *Chemical Physics Letters*, 472(1-3):96–98, 2009.

[73] M.S. Dresselhaus, G. Dresselhaus, A. Jorio, A.G. Souza Filho, and R. Saito. Raman spectroscopy on isolated single wall carbon nanotubes. *Carbon*, 40(12):2043–2061, 2002.

[74] C.A. Hunter and J.K.M. Sanders. The nature of $\pi - \pi$ interactions. *Journal of the American Chemical Society*, 112(14):5525–5534, 1990.

[75] G.R. Desiraju and A. Gavezzotti. From molecular to crystal structure; polynuclear aromatic hydrocarbons. *J. Chem. Soc., Chem. Commun.*, (10):621–623, 1989.

[76] C.A. Hunter, K.R. Lawson, J. Perkins, and C.J. Urch. Aromatic interactions. *Journal of the Chemical Society, Perkin Transactions 2*, (5):651–669, 2001.

[77] A.H.C. Neto, F. Guinea, NMR Peres, K.S. Novoselov, and A.K. Geim. The electronic properties of graphene. *Reviews of Modern Physics*, 81(1):109, 2009.

[78] C. Feng, C.S. Lin, W. Fan, R.Q. Zhang, and M.A. Van Hove. Stacking of polycyclic aromatic hydrocarbons as prototype for graphene multilayers, studied using density functional theory augmented with a dispersion term, 2009.

[79] E. McCann and V.I. Fal'ko. Landau-level degeneracy and quantum hall effect in a graphite bilayer. *Physical review letters*, 96(8):86805, 2006.

[80] K.S. Novoselov, E. McCann, S.V. Morozov, V.I. Fal'ko, M.I. Katsnelson, U. Zeitler, D. Jiang, F. Schedin, and A.K. Geim. Unconventional quantum hall effect and berryâĂŹs phase of 2π in bilayer graphene. *Nature Physics*, 2(3):177–180, 2006.

[81] L.M. Malard, J. Nilsson, DC Elias, J.C. Brant, F. Plentz, E.S. Alves, A.H.C. Neto, and M.A. Pimenta. Probing the electronic structure of bilayer graphene by raman scattering. *Physical Review B*, 76(20):201401, 2007.

[82] K. Nakada, M. Fujita, G. Dresselhaus, and M.S. Dresselhaus. Edge state in graphene ribbons: Nanometer size effect and edge shape dependence. *Physical Review B*, 54(24):17954, 1996.

[83] K. Wakabayashi, M. Fujita, H. Ajiki, and M. Sigrist. Electronic and magnetic properties of nanographite ribbons. *Physical Review B*, 59(12):8271, 1999.

[84] D.C. Elias, R.R. Nair, T.M.G. Mohiuddin, S.V. Morozov, P. Blake, M.P. Halsall, A.C. Ferrari, D.W. Boukhvalov, M.I. Katsnelson, A.K. Geim, et al. Control of graphene's properties by reversible hydrogenation: evidence for graphane. *Science*, 323(5914):610–613, 2009.

[85] N.P. Guisinger, G.M. Rutter, J.N. Crain, P.N. First, and J.A. Stroscio. Exposure of epitaxial graphene on sic (0001) to atomic hydrogen. *Nano letters*, 9(4):1462–1466, 2009.

[86] D.K. Samarakoon and X.Q. Wang. Tunable band gap in hydrogenated bilayer graphene. *ACS nano*, 4(7):4126–4130, 2010.

[87] J.O. Sofo, A.S. Chaudhari, and G.D. Barber. Graphane: A two-dimensional hydrocarbon. *Physical Review B*, 75(15):153401, 2007.

[88] A.R. Badzian, T. Badzian, R. Roy, R. Messier, and K.E. Spear. Crystallization of diamond crystals and films by microwave assisted cvd (part ii). *Materials research bulletin*, 23(4):531–548, 1988.

[89] R.J. Nemanich and J.T. Glass. characterization of carbon bonding in diamond and diamondlike thin films. *Journal of Vacuum Science & Technology A: Vacuum, Surfaces, and Films*, 6,3:1783–1787, 1998.

[90] J. Robertson. Photoluminescence mechanism in amorphous hydrogenated carbon. *Diamond and related materials*, 5(3):457–460, 1996.

[91] J. Robertson. Recombination and photoluminescence mechanism in hydrogenated amorphous carbon. *Physical Review B*, 53(24):16302, 1996.

[92] S.R.P. Silvaf, J. Robertson, Rusli, G.A.J. Amaratunga, and J. Schwan. Structure and luminescence properties of an amorphous hydrogenated carbon. *Philosophical Magazine B*, 74(4):369–386, 1996.

[93] J. Bullot and M.P. Schmidt. Physics of amorphous silicon–carbon alloys. *physica status solidi (b)*, 143(2):345–418, 1987.

[94] F. Demichelis, S. Schreiter, and A. Tagliaferro. Photoluminescence in ac: H films. *Physical Review B*, 51(4):2143, 1995.

[95] J. Robertson and E.P. OâĂŹreilly. Electronic and atomic structure of amorphous carbon. *Physical Review B*, 35(6):2946, 1987.

[96] J. Robertson. Structural models of ac and ac: H. *Diamond and related materials*, 4(4):297–301, 1995.

[97] M. Johnson and R.H. Silsbee. Interfacial charge-spin coupling: Injection and detection of spin magnetization in metals. *Physical review letters*, 55(17):1790–1793, 1985.

[98] M.N. Baibich, J.M. Broto, A. Fert, F. Nguyen Van Dau, F. Petroff, P. Etienne, G. Creuzet, A. Friederich, and J. Chazelas. Giant magnetoresistance of (001)fe/(001)cr magnetic superlattices. *Phys. Rev. Lett.*, 61:2472–2475, Nov 1988.

[99] M. Julliere. Tunneling between ferromagnetic films. *Physics Letters A*, 54(3):225–226, 1975.

[100] S. Datta and B. Das. Electronic analog of the electro-optic modulator. *Applied Physics Letters*, 56(7):665–667, 1990.

[101] Y. Ohno, DK Young, B. Beschoten, F. Matsukura, H. Ohno, and DD Awschalom. Electrical spin injection in a ferromagnetic semiconductor heterostructure. *Nature*, 402(6763):790–792, 1999.

[102] I. Appelbaum, B. Huang, and D.J. Monsma. Electronic measurement and control of spin transport in silicon. *Nature*, 447(7142):295–298, 2007.

[103] M. Ohishi, M. Shiraishi, R. Nouchi, T. Nozaki, T. Shinjo, and Y. Suzuki. Spin injection into a graphene thin film at room temperature. *Arxiv preprint arXiv:0706.1451*, 2007.

[104] Sarxos I.

[105] G.E. Uhlenbeck and S. Goudsmit. Spinning electrons and the structure of spectra. *Nature*, 117:264–265, 1926.

[106] W. Gerlach and O. Stern. Das magnetische moment des silberatoms. *Zeitschrift für Physik A Hadrons and Nuclei*, 9(1):353–355, 1922.

[107] L. De La Peña. *Introducción a la mecánica cuántica*. Fondo De Cultura Economica USA, 2006.

[108] M. Kaku. *Quantum field theory: a modern introduction*, volume 5. Oxford University Press Oxford, 1993.

[109] D.J. Griffiths and E.G. Harris. *Introduction to quantum mechanics*, volume 2. Prentice Hall, 1995.

[110] Gerald Gabrielse and David Hanneke. Precision pins down the electron's magnetism. *CERN Courier*, 48(8):35–37, 2006.

[111] B. Odom, D. Hanneke, B. D'Urso, and G. Gabrielse. New measurement of the electron magnetic moment using a one-electron quantum cyclotron. *Physical review letters*, 97(3):30801, 2006.

[112] U. Barth and L. Hedin. A local exchange-correlation potential for the spin polarized case. i. *Journal of Physics C: Solid State Physics*, 5:1629, 1972.

[113] M.M. Pant and A.K. Rajagopal. Theory of inhomogeneous magnetic electron gas. *Solid State Communications*, 10(12):1157–1160, 1972.

[114] R. Zeller. Spin-polarized dft calculations and magnetism. *Computational Nanoscience: Do It Yourself*, pages 419–445, 2006.

[115] W. Kohn and L. J. Sham. Self-consistent equations including exchange and correlation effects. *Phys. Rev.*, 140:A1133–A1138, Nov 1965.

[116] T. Hahn, U. Shmueli, A.J.C. Wilson, and E. Prince. *International tables for crystallography*. D. Reidel Publishing Company, 2005.

[117] R.M. Martin. *Electronic structure: basic theory and practical methods*. Cambridge university press, 2004.

[118] C. Schönenberger. Bandstructure of graphene and carbon nanotubes: An exercise in condensed matter physics, 2000.

[119] E. Kogan and V.U. Nazarov. Symmetry classification of energy bands in graphene. *arXiv preprint arXiv:1201.5045*, 2012.

[120] J.C. Phillips and L. Kleinman. New method for calculating wave functions in crystals and molecules. *Physical Review*, 116(2):287, 1959.

[121] OH Nielsen and R.M. Martin. Stresses in semiconductors: Ab initio calculations on si, ge, and gaas. *Physical Review B*, 32(6):3792, 1985.

[122] W.E. Pickett. Pseudopotential methods in condensed matter applications. *Computer Physics Reports*, 9(3):115–197, 1989.

[123] J. Ihm, A. Zunger, and M.L. Cohen. Momentum-space formalism for the total energy of solids. *Journal of Physics C: Solid State Physics*, 12(21):4409, 2001.

[124] MT Yin and M.L. Cohen. Theory of ab initio pseudopotential calculations. *Physical Review B*, 25(12):7403, 1982.

[125] M.P. Allen, D.J. Tildesley, and J.R. Banavar. Computer simulation of liquids. *Physics Today*, 42:105, 1989.

[126] J.C. Salazar. Stress modulation of the degree of spin polarization on bulk semiconductors. Master's thesis, CIO, 2009.

[127] X. Gonze. A brief introduction to the abinit software package. *Zeitschrift fur Kristallographie*, 220(5/6/2005):558–562, 2005.

[128] D. Sholl and J.A. Steckel. *Density functional theory: a practical introduction*. Wiley-Interscience, 2011.

[129] J. L. Cabellos, Cuauhtémoc Salazar, and Bernardo S. Mendoza. Stress-modulated optical spin injection in bulk si and gaas semiconductors. *Phys. Rev. B*, 80:245204, Dec 2009.

[130] F. Nastos, J. Rioux, M. Strimas-Mackey, Bernardo S. Mendoza, and J. E. Sipe. Full band structure lda and **k**â**L**Ź**p** calculations of optical spin-injection. *Phys. Rev. B*, 76:205113, Nov 2007.

[131] J.C. Meyer, A.K. Geim, M.I. Katsnelson, K.S. Novoselov, T.J. Booth, and S. Roth. The structure of suspended graphene sheets. *Nature*, 446(7131):60–63, 2007.

[132] R. Seshadri, A. Govindaraj, H.N. Aiyer, R. Sen, G.N. Subbanna, A.R. Raju, and C.N.R. Rao. Investigations of carbon nanotubes. *Current science (Bangalore)*, 66(11):839–847, 1994.

[133] A Ghosh, K Rao, V. George, and S.J. Rao. Non-covalent functionalization, exfoliation and solubilization of graphene in water employing afluorescent coronene carboxylate. *Chemistry–A European Journal*, 16, 2010.

[134] A. Peigney, C. Laurent, E. Flahaut, R.R. Bacsa, and A. Rousset. Specific surface area of carbon nanotubes and bundles of carbon nanotubes. *Carbon*, 39(4):507–514, 2001.

[135] A. Ghosh, K.S. Subrahmanyam, K.S. Krishna, S. Datta, A. Govindaraj, S.K. Pati, and C.N.R. Rao. Uptake of h2 and co2 by graphene. *The Journal of Physical Chemistry C*, 112(40):15704–15707, 2008.

[136] R.Q. Zhang and A. De Sarkar. Theoretical studies on formation, property tuning and adsorption of graphene segments. *Physics and Applications of Graphene–Theory, InTech Openbook*, 2011.

[137] N. Tombros, C. Jozsa, M. Popinciuc, H.T. Jonkman, and B.J. Van Wees. Electronic spin transport and spin precession in single graphene layers at room temperature. *Nature*, 448(7153):571–574, 2007.

[138] S. Cho, Y.F. Chen, and M.S. Fuhrer. Gate-tunable graphene spin valve. *Applied Physics Letters*, 91:123105, 2007.

[139] J. Kessler. *Polarized electrons*, volume 1. Springer, 1985.

Vita

Reinaldo Zapata was born in León, Guanajuato, in 1984. When he and his sisters were just children, their father fell in bed due to a disease. Their lovely mother and the uncle Enrique did everything that was in their hands to give them a good childhood.

He spent his youth in company of his sisters, playing sports, studying, working, traveling in México with his family and collecting music together with Miguel Ochoa, his great friend. When he was studying the school, in the *Instituto América*, he had the opportunity to travel to Chile, together with José M., to study a short time at *Colegio Pierre Faure*. In that place he met some of his best friends: Cecilia Nuñez and Bernardo B.

When he was eighteen he started working at C&A and entered to *Instituto de Física de universidad de Guanajuato*, now called *División de Ciencias e Ingenierías*. Also he took some courses at *Centro de Investigaciones en Óptica A. C.* Two years later he met Patricia García Loza at C&A and felt in love. They were boyfriends for a long time and decided to engage. They got married and have a child. Samantha, their baby girl, came to change and make happy their lives becoming the couple closer together.

Under the tutelage of Dr. José Socorro García (*DCI*) and Moisés Cywiak (*CIO*), and with the help of Moisés Padilla he graduated with "*lauder*" honors receiving the degree in physics and mathematics presenting the thesis *Interferómetro Heterodino de dos Haces Gaussianos para Perfilometría.*

Reinaldo began his masters degree in optical sciences at *Centro de Investigaciones en Óptica* in León, Mexico with Dr. Bernardo Mendoza Santoyo as his advisor. This thesis marks the culmination of that work and was completed on December 2012 with the help of Sean Martin Anderson.

As future perspective Reinaldo is decided to pursue his Ph.D. in theoretical surface optics and spintronics together with scientific parallel computing with the guidance of Dr. Bernardo Mendoza at CIO. One of the interests is the usage and development of free and open source software, following the main principles of the Free Software Foundation and the promotion and distribution of the GNU/Linux free software.